Research Square

Preprints are preliminary reports that have not undergone peer review.
They should not be considered conclusive, used to inform clinical practice,
or referenced by the media as validated information.

Arbitrary-order suppression of source mismatch in photonic entanglement swapping

Annan Chen

annan.chen24@imperial.ac.uk

Imperial College London https://orcid.org/0009-0000-1308-0466

Research Article

Keywords:

Posted Date: November 12th, 2026

DOI: https://doi.org/10.21203/rs.3.rs-11694496/v1

License: This work is licensed under a Creative Commons Attribution 4.0 International License.
Read Full License

Additional Declarations: The authors declare no competing interests.

Arbitrary-order suppression of source mismatch in photonic entanglement swapping

Annan Chen*
Department of Physics, Imperial College London, London, United Kingdom

We establish the minimum number of same-source photons needed for arbitrary-order suppression of source mismatch in photonic entanglement swapping and construct a static passive circuit family that attains it. The result applies to unencoded photons, optics that act identically on all internal states, complete photon-number-resolving detection, and local-unitary recovery of the retained qubits. For two pure source wave packets with squared overlap u, suppressing the bare mismatch error $\epsilon = (1-u)/2$ to order ϵ^r at nonzero ideal success probability requires at least r photons from each source. A cyclic interferometer attains the minimum total of $2r$ photons at every order, with ideal acceptance 2^{2-3r}. An exact transfer expression extends the calculation to distinct wave packets and correlated classical source noise. Near a common wave packet, the leading error is proportional to the summed delayed Hong–Ou–Mandel losses along a closed tour through each source's emissions. For equally spaced emissions, losses that increase concavely with delay select chronological wiring, whereas convex growth selects a folded order; independent fluctuations add the same leading penalty to every wiring. In a Gaussian drift model, folding lowers the smallest reachable error in the compared catalogs by about 23% without adding photons. Including detection, storage, and routing losses, the photon-cost advantage depends on the target and is largest in a narrow target window; at target error 4.35×10^{-4}, the pooled cost is lower by a factor of about 5.6 with equal acceptance and randomization options in both catalogs. A common spectral filter is cheaper in this finite-noise example; a separate pure-source analysis gives a regime with a better cyclic cost exponent.

I. INTRODUCTION

We determine the minimum same-source photon number required at each suppression order and connect the wiring of an attaining circuit family to measurable temporal source correlations. Linear-optical Bell-state measurements (BSMs) swap entanglement between remote qubits by interfering photons emitted from their respective sources [1]. Heralded Bell pairs underpin quantum repeaters [2] and optical interconnects between quantum processors [3]. Residual differences between the internal wave packets limit the quality of the heralded remote state. Two-photon interference between separate GaAs quantum dots has reached visibility $(93.0 \pm 0.8)\%$ without temporal postselection [4], motivating control of source mismatch. For two pure packets and the ideal bare measurement considered here, squared overlap u gives error $\epsilon = (1-u)/2$.

Repeated emissions add a second issue: slow source drift coexists with independent fluctuations, as delayed Hong–Ou–Mandel (HOM) measurements can reveal [5]. Photon number and the assignment of emissions to the circuit therefore enter the same design problem.

Photon distillation improves the indistinguishability of a surviving photon drawn from noisy inputs [6–11]. Marshall's model distills a surviving photon toward a common dominant internal mode, allowing different physical sources and error probabilities [6]. Our starting point is two individually pure sources whose internal wave packets differ. Encoded and ancilla-assisted Bell measurements instead improve measurement success [12, 13]. Recent analyses also follow distinguishability through entangled-state fusion [14] and resolve physical-error responses in photonic seed-state generators [15]. Here the output is a pair of retained remote qubits, and all photons entering the optical instrument are consumed. Each helper photon carries its source's wave packet and is initially uncorrelated with the retained qubits. Coincidence encoding and repetition mechanisms have linear-optical precedents [12, 16, 17]. A single independently prepared auxiliary photon with a controlled internal wave packet can give quadratic suppression [18]. For raw photons drawn directly from the two sources, we seek the photon number required at each suppression order and the wiring that controls drift-induced error.

We prove that every finite static passive network in the stated resource class needs at least r photons from each source for order-r suppression with nonzero ideal acceptance. A cyclic family attains $2r$ photons for every integer $r \geq 1$, with ideal acceptance 2^{2-3r}. For its order-r member, the accepted outcomes retain only the all-correct and all-error contributions, giving Bell weights proportional to $(1-\epsilon)^r$ and ϵ^r. Real source drift breaks the assumption of a common packet within each source. An exact transfer expression then supplies the full accepted remote state for distinct internal product packets and classical correlations. For q photons per source, it requires $O(q)$ contractions once their Gram matrix is given. It retains the complex-overlap information needed in multiphoton interference [19–21]. Near a common packet, the leading error is proportional to the summed delayed-HOM losses along a closed tour through each source's emissions. Choosing the wiring is therefore a tour problem with measurable edge weights. For equally spaced emissions, classical ordering results [22–24] select chronological order when those weights increase concavely

* annan.chen24@imperial.ac.uk

with delay and a folded order when they increase convexly throughout the sampled window.

The finite-noise example connects this wiring rule to achievable error and photon cost. We compare a reference catalog of natural cycles, a Fourier comparator, and bare BSM with an expanded catalog that also includes folded cycles. Folding lowers the smallest reachable error from 4.26×10^{-4} to 3.29×10^{-4}. For a single fixed setting, it removes one photon pair over a target interval of about 3% relative width. Giving both catalogs the same acceptance and randomization options yields a pooled cost reduction of about 5.6 at $\tau_* = 4.35 \times 10^{-4}$, with the largest gains concentrated near that interval. Three noise controls show how the advantage depends on drift correlations and the independent noise floor. A common spectral filter, outside the internal-state-blind resource class, is about 19 times cheaper at this working point. A separate pure-source analysis identifies a regime in which the cyclic family has a better asymptotic photon-cost exponent than this filter baseline.

Sections II–III establish the bound and mechanism, Sec. IV connects wave packets to calibration, and Sec. V evaluates finite-noise costs, including a spectral-filter comparison outside the internal-state-blind resource class.

II. PHYSICAL TASK AND MINIMUM PHOTON NUMBER

A. Inputs, measurement, and resource accounting

A successful optical Bell-state measurement (BSM) should entangle two retained remote qubits, R_A and R_B. Initially each is Bell-paired with a traveling dual-rail data photon. Source $s \in \{a, b\}$ also supplies h_s raw helpers in distinct spatial input modes. Write $n_s = h_s + 1$ and $N = n_a + n_b$; the retained references are excluded from N. The labels A_0, A_1 and B_0, B_1 denote the data photons' dual-rail modes, and $\mathcal{H}_s$ denotes the helper input ports. Additional modes start in vacuum. A retained reference may be a stored partner photon or a matter qubit decoupled from the later helper emissions. The helpers must not carry additional logical correlations with that reference. Table I separates the input assumptions of the photon-number theorem and the finite-noise calculation.

In the pure-source model every photon from source a has normalized internal packet $|a\rangle$, and similarly for b. Define $u = |\langle a|b\rangle|^2$ and bare mismatch error $\epsilon = (1-u)/2$. If $d_j^\dagger(f)$ creates packet f in spatial mode j, the input is

$$|\Psi_{\mathrm{in}}\rangle = \frac{1}{2} \sum_{\alpha,\beta=0}^{1} |\alpha\beta\rangle_{R_A R_B} d_{A_\alpha}^\dagger(a) d_{B_\beta}^\dagger(b) \times \prod_{h\in\mathcal{H}_a} d_h^\dagger(a) \prod_{h\in\mathcal{H}_b} d_h^\dagger(b)|0\rangle. \tag{1}$$

A finite passive unitary $U \in U(M)$ on M spatial modes acts as $d_j^\dagger(f) \mapsto \sum_k U_{kj} d_k^\dagger(f)$ for every internal state. Complete photon-number-resolving (PNR) detection consumes all N interface photons. The record $y = (y_0, \ldots, y_{M-1})$ includes collisions and zero counts, with $\sum_k y_k = N$. Detectors resolve spatial occupations but not the internal wave-packet degrees of freedom, which are traced out.

Let J_y be the unnormalized state of the retained qubits conditioned on y; its trace is the record probability. Retain the record with a fixed probability $\gamma_y \in [0, 1]$ and apply the outcome-dependent local unitary correction $L_y = L_{A,y} \otimes L_{B,y}$. For the target $|\Phi_+\rangle = (|00\rangle + |11\rangle)/\sqrt{2}$, define $\Pi_{\Phi_+} = |\Phi_+\rangle\langle\Phi_+|$ and $\Pi_\perp = I - \Pi_{\Phi_+}$. The accepted state, success probability, error weight, and conditional infidelity are

$$J = \sum_y \gamma_y L_y J_y L_y^\dagger, \qquad P = \mathrm{Tr}\, J,$$
$$Q_{\mathrm{err}} = \mathrm{Tr}(\Pi_\perp J), \qquad E = Q_{\mathrm{err}}/P. \tag{2}$$

An order-r instrument has fixed U, γ_y, L_y, positive ideal probability $P|_{u=1} > 0$, and $E = O(\epsilon^r)$ as $\epsilon \to 0$. Thus r specifies an error-suppression order. The circuit parameter q introduced in Sec. III instead counts slots per source.

For realistic emissions, the internal state in a given classical noise realization is $\bigotimes_{i=0}^{N-1} |\chi_i\rangle$, independent of the logical rails. Data and helpers may all have different packets. A classical mixture of these products allows correlations between emissions and sources. First trace the unresolved internal states for each realization, then average its unnormalized accepted operator:

$$\bar{J} = \mathbb{E}[J], \qquad \bar{P} = \mathrm{Tr}\, \bar{J},$$
$$\bar{Q}_{\mathrm{err}} = \mathrm{Tr}(\Pi_\perp \bar{J}), \qquad \bar{E} = \bar{Q}_{\mathrm{err}}/\bar{P}. \tag{3}$$

Successful trials reweight the noise realizations. Averaging conditional errors, or substituting a mean overlap into a pure-source formula, generally produces a different result.

With independent detection efficiency η, no false counts, and an additional scalar survival s_{loss} that preserves the conditional state, define

$$P_{\mathrm{det}} = \eta^N s_{\mathrm{loss}} \bar{P}, \qquad C = N/P_{\mathrm{det}}. \tag{4}$$

The photon cost C is the long-run number of supplied interface photons per accepted remote pair, for independent trials or a stationary ergodic sequence. The spatial inputs are synchronized by known delays. Source loading and demultiplexing require an additional device-dependent cost model [25]; storage and routing within the specified interface are already included in s_{loss}.

The counted interface assumes complete detection without false counts; Sec. V adds independent detector inefficiency.

TABLE I. Resource scope. The measurement network and input assignment are fixed before each trial. Both descriptions assume that internal states are independent of the logical qubits.

	Photon-number theorem	Finite-noise evaluation
Input	One pure packet per source; unencoded same-source photons	Product packets in each realization; classical mixtures may correlate emissions
Optics	Finite static passive unitary, identical on all internal modes; vacuum extensions allowed	Same static instrument, with calibrated input permutations
Measurement	Complete spatial PNR; nonnegative record retention and local-unitary recovery	Same detection; internal states traced before averaging unnormalized outputs

Outside this resource class: internal-state-selective filters or shifts, pre-encoded logical inputs, and measurement-dependent optical feedforward.

B. A bound for arbitrary allowed passive networks

The following statement applies to the full pure-source resource class of Sec. II, including arbitrary vacuum extensions and nonnegative acceptance weights on complete PNR records.

Theorem 1 (Same-source photon bound)**.** *Let* $m = \min(n_a, n_b)$ *and* $n = \max(n_a, n_b)$. *For* $0 \le u < 1$, *every nonzero accepted operator satisfies*

$$E \ge \frac{(1-u)^m}{\Lambda_{m,n}(u) + (1-u)^m},$$
$$\Lambda_{m,n}(u) = \sum_{k=0}^{m} \binom{m}{k}\binom{n}{k} u^k. \tag{5}$$

An order-r instrument therefore needs $n_a, n_b \ge r$. *The family in Sec. III attains* $N_{\min}(r) = 2r$ *for every integer* $r \ge 1$.

The proof has three steps. Assigning detected positions to their sources gives product reference vectors; their internal-state coherences form a source-assignment Gram matrix $\mathsf{G}^{\mathrm{src}}$. Its eigenvalues lie between $(1-u)^m$ and $\Lambda_{m,n}(u)$. Each product vector has Bell overlap at most half its norm squared, even after a local correction. Combining these facts bounds the error-to-signal ratio of every record; nonnegative record sums preserve the bound. Appendix A gives the complete indexing and spectral argument. Since $\Lambda_{m,n}(1) = \binom{N}{m}$, the leading lower bound is $2^m\epsilon^m/\binom{N}{m}$, excluding $r > m$. The cyclic construction attains the minimum photon number. For equal counts $n_a = n_b = r$, the ratio of its error to the bound tends to $\binom{2r}{r}/2^r$ as $\epsilon \to 0$: 1.5 at $r = 2$ and 4.375 at $r = 4$. Thus finite-error prefactors and the greatest acceptance at order r remain separate optimization questions.

III. A STATIC FAMILY ATTAINING EVERY ORDER

A. Circuit, accepted records, and exact performance

Set $n_a = n_b = q$, $N = 2q$, and $M = 4q$. A spatial mode is (s, j, ℓ), where $s \in \{a, b\}$, $j = 0, \ldots, q-1$, and $\ell = 0, 1$ is the rail. Write $\iota_a = 0, \iota_b = 1$, so its numerical index is $2q\iota_s + 2j + \ell$. Data occupy slot 0; each helper initially occupies rail 0 of a slot $j > 0$, with rail 1 vacuum. The real Hadamard $H = 2^{-1/2}\left(\begin{smallmatrix} 1 & 1 \\ 1 & -1 \end{smallmatrix}\right)$ sets every balanced-mixer phase convention. The complete unitary is

$$U_{\mathrm{cyc}} = B_{\mathrm{cross}} H_{\mathrm{all}} (C_a \oplus C_b) H_{\mathrm{helpers}}. \tag{6}$$

Here H_{helpers} acts on the two rails of each helper and is the identity on data rails. The routing C_s advances rail 1 by one slot modulo q and leaves rail 0 fixed. Then H_{all} acts on every rail pair, and B_{cross} mixes the sources by H at each slot and rail. Its output index $p = 0, 1$ labels a port. Figure 1 shows the retained references, the cyclic selection mechanism, and the achieved error beside the bound. The resolved local mixers are shown in Appendix B.

An opposite-rail record at a slot has one photon in each rail. Equal output ports define sign + and different ports sign −, with two detector patterns per sign. The common-sign, or uniform, class $\mathcal{U}_q$ accepts the same $\varsigma \in \{+, -\}$ at every slot: there are 2^{q+1} complete records, and all others are rejected. For $k_+ = 0, k_- = 1$, the correction is

$$L_\varsigma^{(q)} = Z_A^{q \bmod 2} X_B^{k_\varsigma}. \tag{7}$$

Z_A and X_B are Pauli operators acting on the retained qubits R_A and R_B. Define $A = (1+u)/2 = 1-\epsilon$, $B = (1-u)/2 = \epsilon$, $|\Psi_+\rangle = (|01\rangle + |10\rangle)/\sqrt{2}$, $\Pi_{\Psi_+} = |\Psi_+\rangle\langle\Psi_+|$, and $c_q = 2^{2-3q}$. Then

$$J_{\mathcal{U}_q} = c_q(A^q \Pi_{\Phi_+} + B^q \Pi_{\Psi_+}),$$
$$P_{\mathcal{U}_q} = c_q(A^q + B^q),$$
$$E_{\mathcal{U}_q} = \frac{B^q}{A^q + B^q} = \epsilon^q + O(\epsilon^{q+1}). \tag{8}$$

The $q = 1$ member is the two-photon BSM with $P = 1/2$ and $E = \epsilon$.

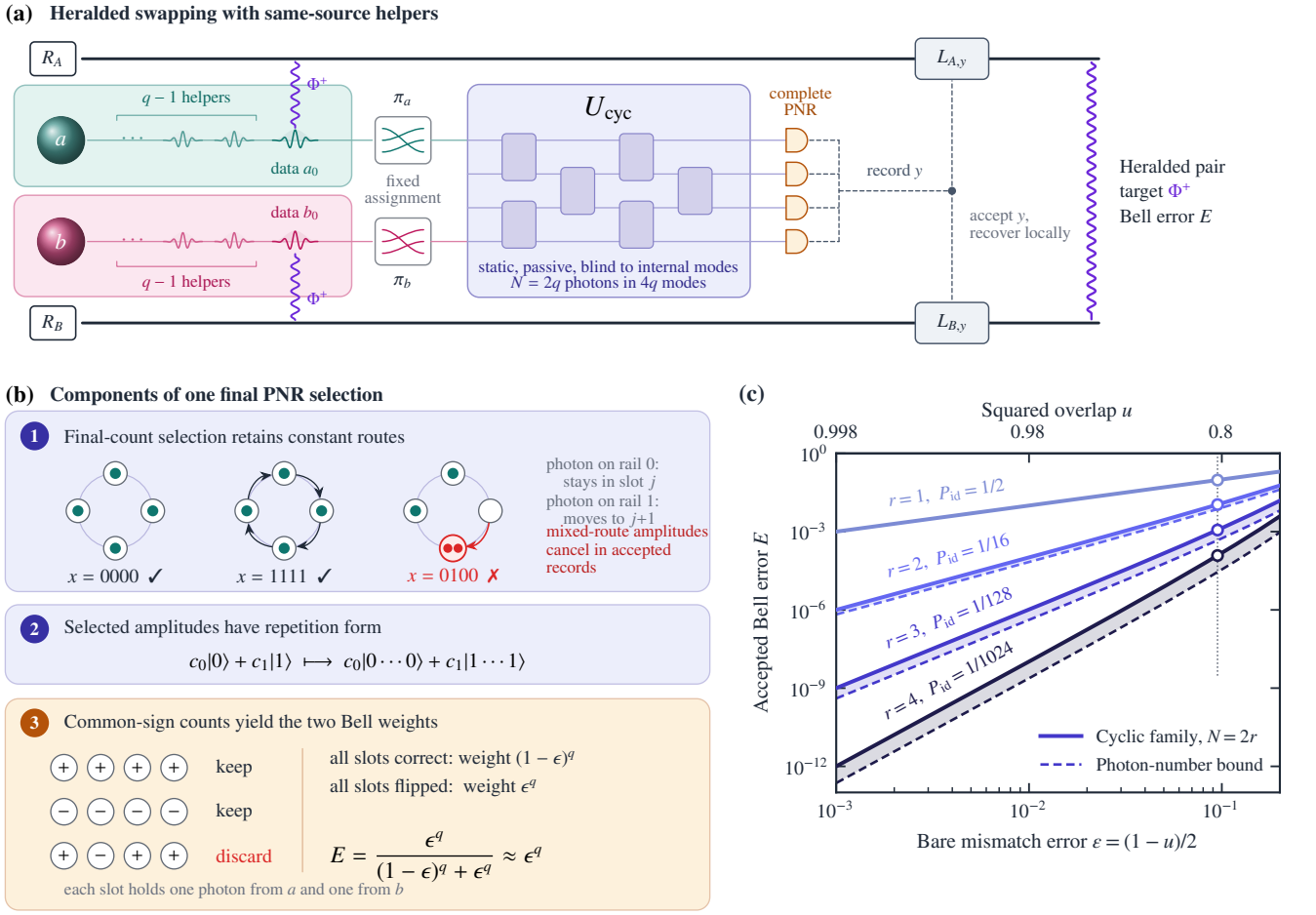


FIG. 1. Same-source photons suppress mismatch in a fixed passive measurement. (a) Source $s \in \{a, b\}$ supplies one data photon, initially Bell-paired with retained reference R_A or R_B, and $q-1$ helpers. The helper assignment π_s fixes the data index, $\pi_s(0) = 0$. The internal-state-blind cyclic network acts on $N = 2q$ photons in $4q$ modes. A complete photon-number-resolving (PNR) record y heralds local corrections $L_{A,y}$ and $L_{B,y}$. (b) Routing components for $q = 4$; the route string x lists bits clockwise from the top slot. Rail 0 stays in its slot and rail 1 advances. Constant routes retain one photon per source slot; the illustrated mixed route has an empty slot and a double occupation removed by Hong–Ou–Mandel (HOM) cancellation in the accepted amplitudes. The surviving source component has repetition form, with logical amplitudes c_0, c_1; its common factor $2^{-(q-1)/2}$ is omitted. For opposite-rail counts, equal output ports give sign + and different ports sign −. A common sign retains the two Bell weights shown. These are components of the same final PNR selection. (c) Exact cyclic error (solid) and the photon-number bound (dashed) for orders $r = 1, \ldots, 4$. Open circles mark the pure-source squared overlap $u = 0.81$; the family attains $N_{\rm min} = 2r$ with ideal acceptance $P_{\rm id} = 2^{2-3r}$.

B. Why the cyclic circuit suppresses mismatch

Final detection selects a repetition component from each source's routing superposition. On that component the common-sign rule retains either q correct or q erroneous signs, producing the powers A^q and B^q. The following routing argument explains why other components cancel. Let $x_j \in \{0, 1\}$ specify whether a source photon stays at slot j or advances to $j + 1$. The occupation of slot j is $1 - x_j + x_{j-1}$. One photon in every slot selects the two constant routing strings. For a data qubit $c_0|0\rangle + c_1|1\rangle$, their contribution before the final local Hadamards is

$$2^{-(q-1)/2}(c_0|0^q\rangle + c_1|1^q\rangle). \tag{9}$$

This linear relation also holds when the data is entangled with its reference. Any other route compatible with the accepted total counts contains a same-source double occupation at some slot. In the pure-source model those photons are identical. Their local Hadamard maps the opposite-rail input into a coherent superposition with both photons in the same rail. Hong–Ou–Mandel (HOM) interference therefore excludes this contribution from the accepted opposite-rail records. All selection and its probability are included in the final complete detection.

On the surviving component, the sign effects have Bell weights A, B. A common sign at all q slots retains A^q, B^q with conditional total probability $2^{-q}(A^q+B^q)$. Including the two sources' combined repetition-component weight

$2^{-2(q-1)}$ gives Eq. (8). Thus the count-optimal family has an exponential acceptance cost:

$$C_{\mathcal{U}_q} = \frac{q}{2s_{\mathrm{loss}}}\left(\frac{8}{\eta^2 A}\right)^q \frac{1}{1+(B/A)^q}. \tag{10}$$

Increasing the ideal order by one divides acceptance by exactly eight. At finite u, successive photon costs also include $(q+1)/q$, losses, and the B/A correction in Eq. (10). In the finite model below, natural $q = 5$ costs about 13.8 times natural $q = 4$. A quality improvement at fixed q can therefore be valuable if it avoids that next pair.

IV. GENERAL WAVE PACKETS AND NOISE-AWARE WIRING

A. A complete finite-noise state

Source drift gives different packets to different emissions. Order photons as $(a_0, \ldots, a_{q-1}, b_0, \ldots, b_{q-1})$ and form their complex Gram matrix $G_{ij} = \langle\chi_i|\chi_j\rangle$. The cyclic connectivity permits an ordered product of fixed-size local transfer matrices. Each entry sums routes compatible with the observed counts, retaining the full overlaps. A boundary map recovers the complete remote state, including its off-diagonal coherences.

Theorem 2 (Finite-wave-packet instrument)**.** *For $q \geq 2$ and any positive-semidefinite unit-diagonal Gram matrix of internal product packets independent of the logical reference, let each $T_j^{(\varsigma)}$ be the 16×16 local transfer matrix and let $\mathcal{B}_q$ reshape sixteen boundary entries into the 4×4 reference operator, including its preparation normalization. The uniform accepted operator is*

$$J_{\mathcal{U}_q} = \sum_{\varsigma=\pm} L_\varsigma^{(q)} \mathcal{B}_q\left[T_1^{(\varsigma)} \cdots T_{q-1}^{(\varsigma)} T_0^{(\varsigma)}\right] L_\varsigma^{(q)\dagger}. \tag{11}$$

Appendix B defines every entry and proves the expression. Classical mixtures use Eq. (3).

The boundary map preserves coherences; a transfer trace alone does not give the remote state. For a given Gram matrix the contraction cost is $O(q)$; constructing source statistics and integrating over noise are separate tasks. The same local construction treats the additional accepted records used in Sec. V.

B. Within-source differences and independent noise

For two pure source packets, the cyclic circuit suppresses their mutual mismatch to order q. Variations between emissions of one source instead contribute at second order in the wave-packet perturbation, or first order in its variance. Wiring determines which pairs of emissions enter.

The permutation $\pi_s(j)$ specifies which chronological emission of source s is placed at spatial slot j, with $\pi_s(0) = 0$ for the data. Its cycle-edge multiset is

$$\mathcal{E}(\pi_s) = \{(\pi_s(j), \pi_s(j+1 \bmod q)) : j = 0, \ldots, q-1\}. \tag{12}$$

The $q = 2$ cycle has two parallel edges.

Near a common normalized ideal packet g, use a dimensionless perturbation parameter ξ and orthogonal tangent vectors $\delta_{s,i} \perp g$: $\chi_{s,i}(\xi) = g + \xi\delta_{s,i} + O(\xi^2)$, with normalization understood. At fixed $q \geq 2$, and with integrable remainders for a classical ensemble, the uniform instrument gives

$$\begin{aligned} \bar{E}_{\mathcal{U}_q} &= \xi^2 R_{\pi_a,\pi_b} + o(\xi^2), \\ R_{\pi_a,\pi_b} &= \frac{1}{8}\sum_{s=a,b}\sum_{(i,j)\in\mathcal{E}(\pi_s)} \mathbb{E}\|\delta_{s,i} - \delta_{s,j}\|^2. \end{aligned} \tag{13}$$

Appendix C derives the single-direction Laplacian and sums orthogonal tangent directions. This includes perturbations of the data photons. At this order a displacement common to every photon from one source contributes zero; the circuit responds to variation within each source batch.

Define source weights $W_{ij}^s = \mathbb{E}\|\delta_{s,i} - \delta_{s,j}\|^2$. For a shared assignment $\pi_a = \pi_b = \pi$, use throughout

$$\begin{aligned} W_{ij} &= W_{ij}^a + W_{ij}^b, \\ F_\pi &= \sum_{(i,j)\in\mathcal{E}(\pi)} W_{ij}, \qquad R_\pi = F_\pi/8. \end{aligned} \tag{14}$$

The two sources need not have the same covariance kernel. If their assignments can be chosen separately, each source cost can instead be minimized separately. For the shared assignment, U_π denotes Eq. (6) preceded by the fixed permutation of input rail pairs that places emission $\pi(j)$ at slot j.

Proposition 3 (Independent-noise penalty)**.** *Write $\delta_{s,i} = d_{s,i} + \zeta_{s,i}$, where the ζ are independent zero-mean tangent fluctuations, independent of d, with $v_{s,i} = \mathbb{E}\|\zeta_{s,i}\|^2$. They add $v_{s,i} + v_{s,j}$ to W_{ij}^s and*

$$R_{\mathrm{floor}} = \frac{1}{4}\sum_{s,i} v_{s,i} \tag{15}$$

to every assignment's leading Bell-error coefficient.

Every vertex has degree two, so even unequal independent variances leave the leading ranking unchanged. They still affect achievable error and the useful photon number.

C. Classical ordering rules and the power-law boundary

Figure 2 shows two assignments of the same emissions. Chronological (natural) order is $\pi_{\mathrm{n}} = (0, 1, \ldots, q-1)$.

Folded order π_{f} lists even indices increasingly and then odd indices decreasingly; for $q = 6$ it is $(0, 2, 4, 5, 3, 1)$. Any tour can be started at the data vertex, so fixing $\pi(0) = 0$ does not restrict the cycle optimization.

For equal emission spacing Δ_{em}, suppose the combined weight is $W_{ij} = w(|i-j|\Delta_{\mathrm{em}})$, and define the integer-lag cost $f(k) = w(k\Delta_{\mathrm{em}})$. Classical tour theory [22–24] gives the following useful classification:

$$F_{\min} = \begin{cases} 2f(1) + (q-2)f(2), & f \text{ convex}, \\ (q-1)f(1) + f(q-1), & f \text{ concave}. \end{cases} \tag{16}$$

Both cases assume nondecreasing f; the second also uses $f(0) = 0$. Folded and natural order attain the respective values. For $q = 2$ both costs are $2f(1)$, and for $q = 3$ the edge sets coincide. Weak curvature need not give a unique optimum. Appendix C 2 gives short equal-spacing proofs.

The two candidate orders can also be compared from three delay weights. For $q \geq 4$ and $f(q-1) > f(1)$, define

$$g_q(k) = \frac{f(k) - f(1)}{f(q-1) - f(1)}. \tag{17}$$

Their difference is

$$F_{\mathrm{n}} - F_{\mathrm{f}} = [f(q-1) - f(1)]\,[1 - (q-2)g_q(2)]. \tag{18}$$

Thus folded order has lower cost than chronological order exactly when $g_q(2) < 1/(q-2)$. Figure 2(c) compares the resulting leading tour costs for the four noise models considered below. If $f(q-1) \leq f(1)$, use the unnormalized difference $f(q-1) - f(1) - (q-2)[f(2) - f(1)]$ directly. Global tour optimality follows from the ordering conditions above; the full instrument evaluates the selected assignments at finite wave-packet mismatch.

Measured or unequal-spacing weights can be checked directly. For $i < j < k < l$, set $c_1 = W_{ij} + W_{kl}$, $c_2 = W_{ik} + W_{jl}$, and $c_3 = W_{il} + W_{jk}$. The Kalmanson conditions $c_1, c_3 \leq c_2$ select natural order; the symmetric off-diagonal Monge (Supnick) conditions $c_1 \leq c_2 \leq c_3$ select folded order. Only the combined weights need satisfy these conditions. Additive independent vertex noise cancels from the four-point comparisons.

For the exact combined-source law $w(t) = c_\nu |t|^{2\nu}$, $0 < \nu \leq 1$, c_ν has units of time$^{-2\nu}$ when tangent norms are dimensionless. A fixed batch window $T = (q-1)\Delta_{\mathrm{em}}$ gives

$$F_{\min} = c_\nu T^{2\nu} \begin{cases} (q-1)^{1-2\nu} + 1, & 0 < \nu < 1/2, \\ 2, & \nu = 1/2, \\ \dfrac{2 + (q-2)2^{2\nu}}{(q-1)^{2\nu}}, & 1/2 < \nu \leq 1. \end{cases} \tag{19}$$

The Bell coefficient remains $R_{\min} = F_{\min}/8$. The increment-scaling exponent ν equals the Hurst parameter for a fractional Brownian model. Diffusive increments have $\nu = 1/2$ at short delays, while smooth drift has $\nu = 1$ locally. A finite-correlation process need not follow one power law over the full batch. Equation (19) holds the batch window fixed. At fixed emission spacing, adding photons instead extends that window and samples more drift, which can offset higher-order mismatch suppression. These are leading coefficients at fixed q.

D. From HOM calibration to a finite-noise decision

A calibrated balanced HOM experiment on pairs of emissions from the same source estimates the ensemble-averaged visibility $\mathbb{E}[V_{ij}^s]$, where $V_{ij}^s = |\langle \chi_{s,i} | \chi_{s,j} \rangle|^2$ for an individual realization.

At the common ideal point,

$$\begin{aligned} 1 - \mathbb{E}V_{ij}^s &= \xi^2 W_{ij}^s + o(\xi^2), \\ \bar{E}_{\mathcal{U}_q} &= \frac{1}{8} \sum_s \sum_{(i,j) \in \mathcal{E}(\pi_s)} (1 - \mathbb{E}V_{ij}^s) \\ &\quad + o(\xi^2). \end{aligned} \tag{20}$$

Delayed HOM measurements probe temporal correlations directly [5]. Protocol 1 turns that measurement into a fixed instrument design.

Finite-noise evaluation also requires collective Gram phases and higher ensemble moments, supplied by additional source characterization or an explicit physical model [20]. Appendix C 3 gives uncertainty bounds and model-generated examples with unequal times and source noise. The assignment is fixed in advance from calibration.

At the finite source mismatch used below, the common-packet ordering rule generates candidate assignments; their errors and costs are evaluated with the full Gram matrix. The finite-u response in Appendix C applies to perturbations orthogonal to both source packets, whereas Gaussian frequency shifts need not satisfy that condition.

V. FINITE-NOISE ERRORS AND FAIR RESOURCE FRONTIERS

A. Spectral ensemble and losses

Use an illustrative model of synchronized Gaussian packets, with spectral intensity standard deviation σ:

$$\begin{aligned} \chi_\Omega(\omega) &= (2\pi\sigma^2)^{-1/4} e^{-(\omega-\Omega)^2/(4\sigma^2)}, \\ G_{ij} &= e^{-(\Omega_i - \Omega_j)^2/(8\sigma^2)}. \end{aligned} \tag{21}$$

The spectral coordinate ω, packet center Ω, and σ use the same frequency units. At $t_j = j\Delta_{\mathrm{em}}$, let $\Omega_{s,j} = \mu_s + d_s(t_j) + f_{s,j}$, where μ_s is the mean center. The zero-mean slow drift is jointly Gaussian with same-source covariance $\sigma_d^2 \mathcal{R}(t_i - t_j)$ and cross-source covariance $\rho\sigma_d^2 \mathcal{R}(t_i - t_j)$, where $\rho \in [-1, 1]$ is the cross-source correlation coefficient. The fast offsets $f_{s,j}$ are mutually

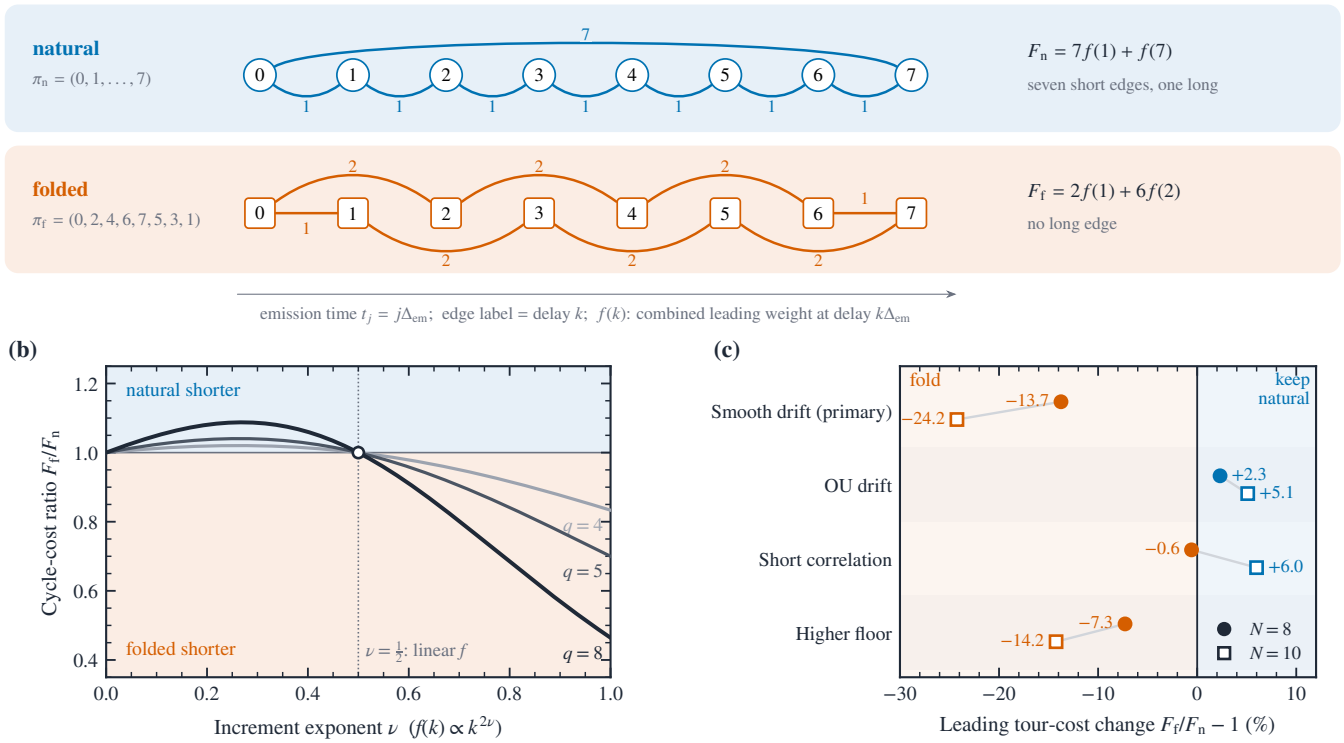


FIG. 2. Delayed-HOM information selects candidate wiring orders. (a) Natural and folded closed tours at $q = 8$ on the same emission times. Edge labels give the delay in units of Δ_{em}; $f(k)$ is the combined leading weight at delay $k\Delta_{em}$. (b) Leading cost ratios for $f(k) \propto k^{2\nu}$ at $q = 4, 5, 8$; the curvature boundary is $\nu = 1/2$. (c) Changes $100(F_f/F_n - 1)$ for the primary smooth drift and three controls of Sec. V, at $N = 8$ (filled circles) and $N = 10$ (open squares). Negative values favor folded wiring; positive values favor natural wiring. An independent additive leading floor leaves this ordering unchanged but dilutes the relative percentage. Only these two candidate tours are compared; the full Gram instrument determines their finite-noise errors in Fig. 3(b).

Protocol 1. From delayed HOM data to fixed wiring

Input. Ensemble-averaged delayed-HOM visibilities at the actual batch delays, calibration uncertainties, and a model or characterization of the full source statistics.

1. Calibrate and form weights. Match batch conditions; correct instrumental visibility loss. Form source-resolved W^s_{ij} or shared-assignment $W_{ij} = W^a_{ij} + W^b_{ij}$ and propagate uncertainties. For equal spacing only, write the stationary combined weights as $f(k)$.

Chronological candidate
Equal spacing: nondecreasing, concave f, with $f(0) = 0$.
General weights:
Kalmanson four-point conditions.

Unresolved conditions
Compare candidate tour costs directly.
Equal spacing: the three-delay difference compares natural and folded tours.

Folded candidate
Equal spacing: nondecreasing, convex f.
General weights:
Supnick four-point conditions.

2. Evaluate candidate assignments. Use the full Gram ensemble; average the unnormalized operators, then normalize over successful trials. Include detection, storage, and routing losses in the photon cost.

Output. Source-to-slot assignments π_s fixed before the trials, accepted errors $\bar{E}$, and photon costs per accepted pair. Leading-order ordering selects candidates; the complete instrument determines their finite-noise performance.

independent zero-mean Gaussian variables across photons and sources, with variance σ_f^2 on data and helpers, and are independent of the slow drift processes $d_s(t)$. The smooth correlation kernel is $\mathcal{R}(t) = e^{-t^2/(2T_c^2)}$, with correlation time T_c; an Ornstein–Uhlenbeck (OU) control uses $e^{-|t|/T_c}$. A squared-exponential spectral-diffusion model has been used to describe delayed-HOM data [5]. Its convention $e^{-(t/\tau_c)^2}$ corresponds to $\tau_c = \sqrt{2}T_c$ here. This motivates the correlation structure; the parameters below are illustrative, not a fit to that experiment.

The primary model has

$$\begin{aligned} u_{\mathrm{nom}} &= e^{-(\mu_a-\mu_b)^2/(4\sigma^2)} = 0.81, \qquad \rho = 0, \\ \sigma_d/\sigma &= 0.1, \quad \sigma_f/\sigma = 0.005, \quad T_c/\Delta_{\mathrm{em}} = 6. \end{aligned} \tag{22}$$

Here u_{nom} is the squared overlap at the mean centers; individual overlaps fluctuate. The emission spacing is fixed, so $T = (q-1)\Delta_{\mathrm{em}}$ grows with q. For small frequency separations the exact overlap obeys

$$1 - |G_{ij}|^2 = \frac{(\Omega_i - \Omega_j)^2}{4\sigma^2} + O\left(\frac{(\Omega_i - \Omega_j)^4}{\sigma^4}\right). \tag{23}$$

In the common-packet limit, homogeneous independent frequency noise thus contributes $q\sigma_f^2/(8\sigma^2)$ to the leading Bell error. For the identical source statistics used in Fig. 2(c), the combined leading weights are proportional to $(\sigma_d/\sigma)^2[1 - \mathcal{R}(k\Delta_{\mathrm{em}})] + (\sigma_f/\sigma)^2$. The common scale and additive floor cancel in g_q, while the floor still contributes to the absolute error. All results at $u_{\mathrm{nom}} = 0.81$ use the full Gram matrix in Eq. (21).

In the serial synchronization model, every photon waits for the last emission. The two sources accumulate total waiting time $q(q-1)\Delta_{\mathrm{em}}$. Frequency-flat attenuation at rate κ, detection efficiency $\eta = 0.9$, and per-photon route survival $\eta_{\mathrm{route},i}$ give, for a cycle setting i,

$$P_{\mathrm{det},i} = \eta^{2q_i} e^{-\kappa q_i(q_i-1)\Delta_{\mathrm{em}}} \eta_{\mathrm{route},i}^{2q_i} \bar{P}_i. \tag{24}$$

We use $\kappa\Delta_{\mathrm{em}} = 0.002$ and $\eta_{\mathrm{route},i} = 1$ for natural wiring or 0.995 for folded wiring. We assign folded wiring an additional 0.5% loss per photon as a conservative model penalty.

The six-photon comparator pays the same $q = 3$ storage and detection costs, with unit extra route survival. Appendix D derives this scalar loss law for equal transmission on both logical rails. Frequency-selective loss or dephasing would require a changed state calculation.

B. Comparison catalogs, quality improvement, and controls

As a working target for the conditional infidelity, we use $\tau_* = 4.35 \times 10^{-4}$, inside the window where the listed natural and folded settings require different photon numbers (Sec. V D).

To compare resources fairly, both catalogs retain all declared acceptance options. Besides the uniform rule $\mathcal{U}_q$, the one-exception class $\mathcal{V}_q$ accepts one same-rail slot and a common opposite-rail sign elsewhere. Its dark subset $\mathcal{D}_q$ keeps only the two split-port patterns at that slot; their ideal probability vanishes. Appendix B 3 defines the records and recoveries, including the unions $\mathcal{U}_q \cup \mathcal{V}_q$ and $\mathcal{U}_q \cup \mathcal{D}_q$. The reference catalog contains natural cycles $q = 2, \ldots, 8$ with these five rules, bare BSM, and the six-photon Fourier comparator with five fixed acceptance choices $\mathcal{Q}_k$, $k = 0, \ldots, 4$. Here $\mathcal{Q}_0$ accepts one photon in each of the six Fourier outputs and none in the four reject modes; the other choices add prescribed records with fixed retention probabilities. The expanded catalog adds folded cycles with the same sizes and rules. Both may use the same freedom to randomize. The comparator is the ten-mode Fourier-column construction with fixed acceptance rules specified in Appendix E.

Figure 3 shows the quality mechanism. At $N = 8$, folding lowers the error under the uniform acceptance rule by 7.95%, from 4.40×10^{-4} to 4.05×10^{-4}; at $N = 10$ the improvement is 22.8%. The $N = 8$ optical acceptances agree to the displayed precision, $\bar{P} = 6.549 \times 10^{-4}$. These improvements add no photons, but the route attenuation makes fixed-size costs about 4.1% and 5.1% higher, respectively. Savings arise when the improved error permits a smaller circuit to meet a target. In the primary model the error is lowest at $q = 5$: adding another pair suppresses pure-source mismatch but lengthens the batch window and exposes more drift.

The controls test which drift structure supports the gain. OU drift favors natural wiring at both sizes. Short correlation gives a small $N = 8$ improvement but worsens $N = 10$; the two full catalog frontiers coincide for OU and short correlation, and neither reaches τ_*. A larger independent floor retains fixed-size quality improvements while also making this target unreachable. Under all four models the leading cycle-cost comparison and the full finite-noise calculation agree on the sign of the change at $q = 4, 5$, a diagnostic rather than a finite-u theorem.

Fourier $\mathcal{Q}_0$ has primary error 7.30×10^{-4} and participates in pooled resource mixtures. The other four Fourier sets stay in both catalogs even though they do not support the primary frontier. One-exception unions enter the relaxed-target frontier at natural $q = 3, 2$; dark extensions do not. The complete catalog and control values remain in Appendix F.

Figure 4 shows how the target changes the lowest cost in each catalog. Its pooled curves allow random selection of settings before each attempt, as specified next.

C. Strategy choices and successful-event weights

Table II distinguishes three resource tasks with the same options on both sides. The pooled task constrains mean infidelity over all delivered accepted pairs. If a downstream task requires each known setting label to meet the target individually, the single-setting comparison applies instead.

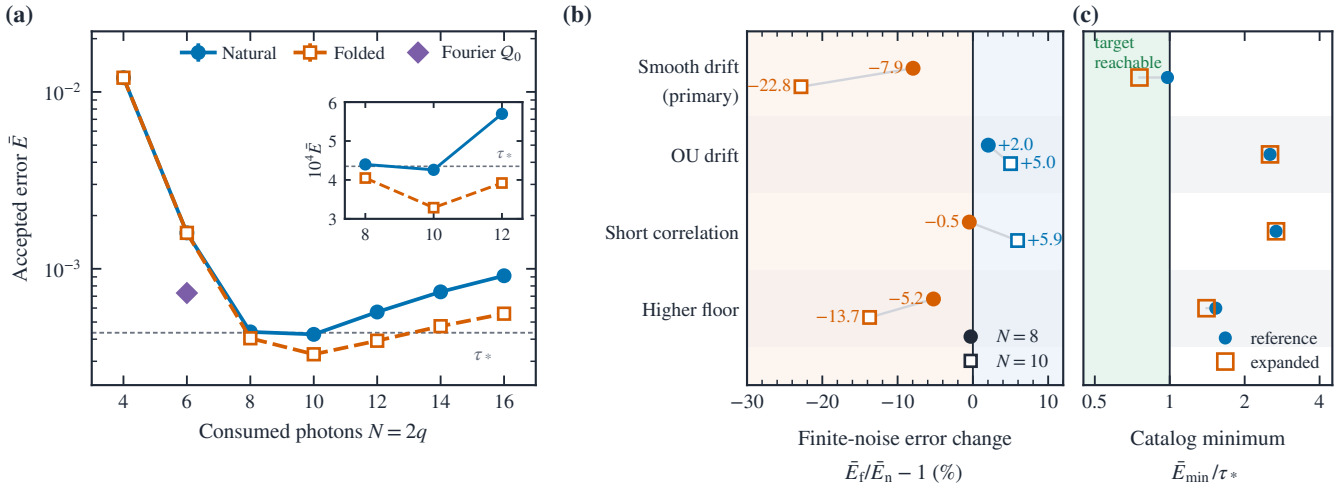


FIG. 3. Finite-noise quality and target feasibility. (a) Primary errors under the uniform acceptance rule and the Fourier comparator $\mathcal{Q}_0$, with an inset around $\tau_* = 4.35 \times 10^{-4}$. Error bars are standard errors across independently randomized Sobol integrations and are often smaller than the markers. (b) Changes $100(\bar{E}_f/\bar{E}_n - 1)$ at fixed $N = 8$ (filled circles) and $N = 10$ (open squares). Orange denotes a decrease and blue an increase. Horizontal error bars are paired jackknife standard errors in percentage points, all below 0.034. Primary means use eight randomized integrations of 4096 points; controls use four of 1024. (c) Minimum error in each finite catalog divided by τ_*; the shaded region is feasible. The expanded catalog includes all reference settings, so its minimum error cannot exceed the reference minimum. Controls change only the kernel to OU, T_c/Δ_{em} to 2, or σ_f/σ to 0.02. Full control responses and paired values are in Appendix F.

TABLE II. Equal strategy options at $\tau_* = 4.35 \times 10^{-4}$. Costs are in units of 10^4 supplied photons per accepted pair. The first row selects one listed circuit and acceptance rule. The second allows partial acceptance within a fixed network. The third randomizes between listed settings and constrains the delivered mean error. Both catalogs have the same options in each row.

Strategy	Ref. $C/10^4$	Exp. $C/10^4$	Ratio
Listed setting	40.2	3.03	13.3
Fixed network	39.5	2.96	13.3
Pooled settings	15.9	2.86	5.57

For setting i, define its detected unnormalized state by

$$J_i^{\mathrm{det}} = \eta^{N_i} s_{\mathrm{loss},i} \bar{J}_i, \quad P_{\mathrm{det},i} = \mathrm{Tr}\, J_i^{\mathrm{det}}, \quad C_i = N_i/P_{\mathrm{det},i}, \tag{25}$$

and set $e_i = \bar{E}_i$. Choose i before each attempt with probability a_i, independently of the instantaneous noise and detection result. Its share among accepted events is $w_i = a_i P_{\mathrm{det},i}/\sum_j a_j P_{\mathrm{det},j}$. A more successful setting contributes more to the accepted sample than its fraction of attempts. Directly averaging the detected states and supplied counts gives

$$E_{\mathrm{mix}} = \sum_i w_i e_i, \qquad C_{\mathrm{mix}} = \sum_i w_i C_i,$$
$$a_i = \frac{w_i/P_{\mathrm{det},i}}{\sum_j w_j/P_{\mathrm{det},j}}. \tag{26}$$

The numerator count per attempt is $\sum_i a_i N_i$, and the success probability is $\sum_i a_i P_{\mathrm{det},i}$.

For a target conditional infidelity τ, minimizing C_{mix} subject to $E_{\mathrm{mix}} \le \tau$ is a linear program in the success weights. Its optimum is on the lower convex frontier of (e_i, C_i) in linear coordinates. Normalization and at most one active error constraint imply an optimum with at most two support settings, a standard linear-programming fact [26]. Equation (26) gives their actual attempt probabilities. Appendix F 2 states the optimization and its supporting-line check. Any additional switching or loading overhead must enter the setting costs before forming the frontier.

D. Target-dependent resource gains

Quality improvement translates into savings relative to an error target. Let $e_{\mathrm{n},q}$ denote the primary mean error of the natural uniform setting with q photons per source. A single listed natural setting needs ten photons throughout

$$e_{\mathrm{n},5} \le \tau < e_{\mathrm{n},4}, \tag{27}$$

where $e_{\mathrm{n},5} \simeq 4.260 \times 10^{-4}$ and $e_{\mathrm{n},4} \simeq 4.398 \times 10^{-4}$, and the eight-photon folded setting is already feasible. Throughout this half-open interval the single-setting cost ratio is 13.297.

At the upper endpoint natural $q = 4$ becomes feasible and that ratio drops to one. Figure 4 instead shows the pooled ratio changing continuously across this window, from about 13.82 to 1.025. A ratio is undefined where the reference is infeasible.

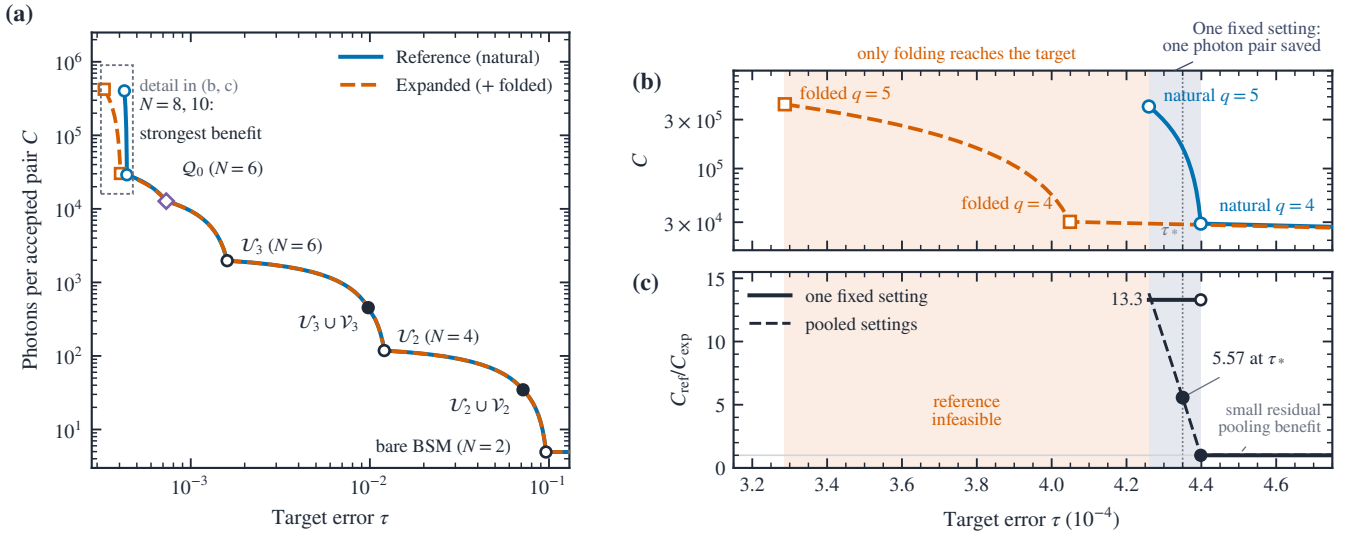


FIG. 4. Target-dependent photon costs with equal acceptance and randomization options. (a) Full pooled frontiers, including Fourier $\mathcal{Q}_0$, uniform rules $\mathcal{U}_q$, one-exception unions $\mathcal{U}_q \cup \mathcal{V}_q$, and bare BSM. The boxed region, where the largest cost reductions occur, is enlarged in (b,c). Costs interpolate in physical linear $(\bar{E}, C)$ coordinates before logarithmic display. (b) Pooled costs near the reachable-error boundary. The expanded catalog reaches 3.287×10^{-4}, below the reference minimum 4.260×10^{-4}. The gray band is the half-open interval in Eq. (27) where one fixed setting saves one photon pair. (c) Cost ratios are defined only where both catalogs are feasible. The single-setting ratio (solid) is 13.297 inside the gray band; open and filled endpoints show its jump to one at the upper boundary. The pooled ratio (dashed) is still 1.02456 there and 1.02417 at 4.5×10^{-4}; the two pooled frontiers merge only at $\mathcal{Q}_0$, with error 7.2954×10^{-4}. At $\tau_* = 4.35 \times 10^{-4}$, the primary pooled ratio is 5.57; the independent refinement gives 5.48.

At τ_* the primary pooled costs are 1.59×10^5 and 2.86×10^4, giving 5.57. Reference mixes natural uniform $q = 5, 4$; expanded mixes folded uniform $q = 4$ and Fourier $\mathcal{Q}_0$. Their mean photon counts per attempt are 9.71 and 7.89. Among the three displayed comparisons, pooling yields the smallest ratio because it reduces the reference cost substantially. Independent 8192-point estimates of the decisive $q = 4, 5$ means give 5.48; the primary data and this refinement remain separate in Appendix F.

Across sixteen calibration corners, the $q = 4$ folded-to-natural error ratio stays between 0.919 and 0.922. Natural $q = 4$ meets τ_* at five corners, and natural $q = 5$ fails at four. The quality improvement persists in these tests, while the cost ratio at a fixed target is sensitive to calibration.

E. Comparison with a common spectral filter

Internal-state-selective operations provide a useful application baseline. Apply the same amplitude filter $H_F(\omega) = \exp[-(\omega - \omega_F)^2/(4\sigma_F^2)]$ to both logical rails of each data photon, with unit peak intensity transmission and center $\omega_F = (\mu_a + \mu_b)/2$, then perform bare BSM. In the same primary Gaussian ensemble and at the same $\eta = 0.9$, transmission-weighted analytic averaging gives $\sigma_F/\sigma = 0.0643$ and $C_F \simeq 1492$ at τ_*. Failed transmissions are included. This is about 19.2 times below the expanded catalog cost and 106.8 times below reference. Appendix F 4 gives the formulas.

Appendix F 4 also identifies a regime in which the cyclic family has an asymptotic photon-cost advantage over this Gaussian-filter baseline. For fixed pure-source squared overlap $0 < u < 1$ and detection efficiency, with no storage or extra routing loss, its cost grows more slowly as the target error tends to zero when $8\epsilon < \eta^2(1 - \epsilon)^2$. At $\eta = 0.9$, this requires $\epsilon < 0.0848$ (approximately $u > 0.8304$). The primary model has nominal $\epsilon = 0.095$; its finite-noise cost comparison above also includes source fluctuations and size-dependent storage loss.

The wiring gain quantifies an advantage within the internal-state-blind catalogs. Filtering changes the internal-state operation and is outside Theorem 1, while remaining a meaningful cost competitor. Its transform-limited pulse duration increases by a factor of about 15.6 at the primary filter setting. A throughput comparison would need the same timing and memory model on both sides; that factor is not multiplied into the photon-count cost.

VI. DISCUSSION AND CONCLUSION

Static internal-state-blind passive optics and complete photon counting can suppress pure-source mismatch to every order. At order r, at least r photons from each source are necessary, and the cyclic family achieves that count with an explicit acceptance price. Optimal finite-

error prefactors and optimal acceptance at fixed order remain open within this resource class.

The full wave-packet instrument connects the ideal statement to drifting sources. Its common-packet expansion reduces the wiring choice to a tour with edge weights measured by delayed HOM interference. Classical ordering results solve the structured concave and convex cases, and independent noise adds the same leading penalty to every cycle. The full source statistics, successful-trial weighting, and losses then determine quality and target-dependent cost at the operating point.

The four-photon member already exhibits the mechanism: for pure source packets with $u = 0.9$, $q = 2$ gives $E = 0.002762$ and optical acceptance $P = 0.05656$. Existing demultiplexing technology [25] motivates the photon number, but a full implementation must also preserve data-reference entanglement while supplying logically independent helpers, synchronize them, and resolve complete photon counts. The two permutations can share a loading interface; actual delays and routing losses require a device model. Internal–logical correlations require an enlarged input model.

For sequential-emission sources, delayed-HOM calibration can select candidate input assignments before the full instrument evaluates their Bell-pair errors and photon costs. Combining these steps with a device-specific loading and loss model could guide the choice of photon number and wiring for photonic interfaces in quantum repeaters or modular quantum processors.

In the primary finite-noise model, a common spectral filter is about 19 times cheaper than the expanded catalog. The separate pure-source analysis identifies when the cyclic family has a better asymptotic cost exponent. These results locate the resource advantage and the importance of the allowed internal-state operations.

Useful next questions are the largest acceptance at fixed suppression order, better finite-error prefactors, and costs when specified internal-state control, pre-encoding, or resource reuse is allowed. The present general product-ensemble description can already evaluate non-Gaussian classical noise; device-calibrated statistics and resource accounting will determine which realization is useful.

FUNDING

The author received no specific funding for this work.

COMPETING INTERESTS

The author declares no competing interests.

DATA AVAILABILITY

The data and code supporting this study are openly available in the Zenodo archive [27] at 10.5281/zenodo.23990533.

Appendix A: Proof of the same-source photon bound

Relabel sources so that $n_a = m$. List a record's detected positions, with spatial rows repeated according to y, and put $m_y = \prod_k y_k!$. For each m-subset S of these N detected positions, write y_S for the sublist of repeated output rows at positions in S. Write per for the permanent and define the reference column

$$\begin{aligned} a_S &= \big(\operatorname{per} U[y_S; A_\alpha, \mathcal{H}_a]\big)_{\alpha=0,1}, \\ b_{S^c} &= \big(\operatorname{per} U[y_{S^c}; B_\beta, \mathcal{H}_b]\big)_{\beta=0,1}, \\ v_S &= (a_S \otimes b_{S^c})/(2\sqrt{m_y}). \end{aligned}$$

Each column is a product vector; repeated rows and m_y include collisions. Grouping bosonic assignments by source gives the following representation. For two assignments S, S', the internal trace is $\langle a|b\rangle^{|S\setminus S'|}\langle b|a\rangle^{|S'\setminus S|} = u^{m-|S\cap S'|}$, since both differing sets have size $m-|S\cap S'|$. Let V_y be the matrix whose columns are v_S. Then $J_y = V_y \mathsf{G}^{\mathrm{src}}_{m,n}(u) V_y^\dagger$, where $[\mathsf{G}^{\mathrm{src}}]_{SS'} = u^{m-|S\cap S'|}$. This is a source-assignment Gram matrix, distinct from the photon Gram used below.

Let $\mathsf{I}_j[T,S] = 1[T \subseteq S]$ for j-subsets T. The binomial identity

$$\mathsf{G}^{\mathrm{src}} = \sum_{j=0}^{m} u^{m-j}(1-u)^j \mathsf{I}_j^T \mathsf{I}_j \succeq (1-u)^m I$$

uses $\mathsf{I}_m = I$; $\succeq$ denotes positive-semidefinite matrix order. Nonnegative entries and the constant row sum give $\mathsf{G}^{\mathrm{src}} \preceq \Lambda_{m,n} I$. The inclusion-matrix structure is standard [28]; these two bounds follow directly from the displayed identities. The Bell-error estimate follows from the product-column spectral bound [29].

After recovery, let $D_y = L_y V_y V_y^\dagger L_y^\dagger$. Write $D = D_y$. For any product vector $x \otimes y$, Cauchy–Schwarz gives

$$|\langle \Phi_+ | x \otimes y\rangle|^2 = \tfrac{1}{2}|x_0 y_0 + x_1 y_1|^2 \le \tfrac{1}{2}\|x\|^2\|y\|^2.$$

Local-unitary recovery preserves the product form. Summing the product projectors gives $\operatorname{Tr}(\Pi_{\Phi_+} D) \le \operatorname{Tr}(\Pi_\perp D)$. For the error projection the matrix $X = V_y^\dagger L_y^\dagger \Pi_\perp L_y V_y$ is positive semidefinite; therefore $\operatorname{Tr}(\mathsf{G}^{\mathrm{src}} X) \ge (1-$

$u)^m \operatorname{Tr} X$. Hence, writing the recovered Bell signal as S_{sig},

$$\begin{aligned} Q_{\mathrm{err}} &\geq (1-u)^m \operatorname{Tr}(\Pi_\perp D), \\ S_{\mathrm{sig}} &\leq \Lambda_{m,n} \operatorname{Tr}(\Pi_{\Phi_+} D) \\ &\leq \Lambda_{m,n} \operatorname{Tr}(\Pi_\perp D). \end{aligned}$$

The ratio $Q_{\mathrm{err}}/(Q_{\mathrm{err}} + S_{\mathrm{sig}})$ gives (5). Positive sums of recovered records, including dark records, preserve the same inequality. Finally $\Lambda_{m,n}(1) = \binom{N}{m}$, so the bound is $2^m \epsilon^m / \binom{N}{m} + O(\epsilon^{m+1})$. It excludes $r > m$.

Appendix B: Exact local tensors and accepted records

1. Photon lists, local outputs and normalization

Figure 5 resolves the local mixing layers of Eq. (6). Before assignment, photons are ordered as $(a_0, \ldots, a_{q-1}, b_0, \ldots, b_{q-1})$, with data at index zero and $G_{ij} = \langle \chi_i | \chi_j \rangle$. For assignments $\pi_s(0) = 0$, form the Gram matrix in circuit-slot order,

$$G^{\pi}_{(s,j),(s',k)} = G_{(s,\pi_s(j)),(s',\pi_{s'}(k))}.$$

Below, j labels a circuit slot; we use this permuted Gram matrix and omit the superscript π. For source $s \in \{a, b\}$, route $x_{s,j} = 0$ stays at slot j and route 1 advances to $j+1$ modulo q. A source's helper preparation has equal amplitudes for these routes; the data route is fixed by its reference logical index. For previous and current routes x', x, define the ordered list

$$I_j(x', x) = \{(s, j, 0) : x_s = 0\} \cup \{(s, j-1, 1) : x'_s = 1\}. \tag{B1}$$

An item (s, i, x) records the source, the input slot of its photon, and the routed rail; (s, i) selects that photon's row or column in the permuted Gram matrix. All slot indices are taken modulo q. Only two-element lists can yield an accepted two-photon local record.

The final rail Hadamard and source mixer give $b_{\mathrm{loc},(p,\ell),(s,x)} = (-1)^{p\iota_s + \ell x}/2$. For ket list I^{k}, bra list I^{b}, outputs o_0, o_1, and local output factorial $m_o = 2$ if $o_0 = o_1$ and 1 otherwise, let S_2 be the permutation group of the two detected positions. The local density factor is

$$\begin{aligned} \mathcal{L}(I^{\mathrm{k}}, I^{\mathrm{b}}; o_0, o_1) = \frac{1}{m_o} \sum_{\alpha,\beta \in S_2} \prod_{t=0}^{1} b_{o_t, I^{\mathrm{k}}_{\alpha(t)}} \overline{b_{o_t, I^{\mathrm{b}}_{\beta(t)}}} \\ \times \prod_{t=0}^{1} G_{I^{\mathrm{b}}_{\beta(t)}, I^{\mathrm{k}}_{\alpha(t)}}. \end{aligned} \tag{B2}$$

The symbol b abbreviates b_{loc}; Gram indices use photon identities only. Both S_2 sums are retained even for a repeated output. The division by its Fock factorial is performed exactly once.

Index the four ket routes by $2x_a + x_b$ and the ket–bra route pairs by $v = 4(2x^{\mathrm{k}}_a + x^{\mathrm{k}}_b) + (2x^{\mathrm{b}}_a + x^{\mathrm{b}}_b)$. Define v' analogously for the preceding slot. The matrix entry $T^{(\varsigma)}_j[v', v]$ uses the lists from the ket and bra cuts in (B1). Its detector patterns are $((p,0),(p,1))$ for sign $+$, or $((p,0),(1-p,1))$ for sign $-$, summed over $p = 0, 1$. These outputs are always distinct, so $m_o = 1$ for the uniform class. Impossible occupations give a zero tensor entry.

2. Proof of the transfer formula

Expand all $2(q-1)$ helper Hadamards into routing choices. At a data cut, a logical ket index $l = 2\alpha + \beta$ fixes $x_{a,0} = \alpha$, $x_{b,0} = \beta$; a logical bra index $k = 2\alpha' + \beta'$ fixes their primed values independently. The routing permutation sends exactly the photons of (B1) to slot j. A record accepts precisely two there; all other list sizes are projected out.

Each allowed slot has two ways to assign its ket photons and two for its bra photons to the detected positions. The trace over unresolved internal outputs is the product of the two Gram overlaps in (B2). This includes their complex phases. Distinct detector patterns add incoherently, so the port sum is local while the common global sign remains fixed. Ordinary matrix multiplication sums every unfixed double route once:

$$\mathcal{P}_\varsigma = T^{(\varsigma)}_1 \cdots T^{(\varsigma)}_{q-1} T^{(\varsigma)}_0.$$

Closing the circuit at the data cut requires the same fixed double route at the two ends. Hence the full raw reference operator is

$$[J^{\mathrm{raw}}_\varsigma]_{lk} = 4^{-q} [\mathcal{P}_\varsigma]_{4l+k, 4l+k}. \tag{B3}$$

Equation (B3) defines the boundary map $\mathcal{B}_q$ in Theorem 2. It reshapes sixteen entries instead of tracing them;

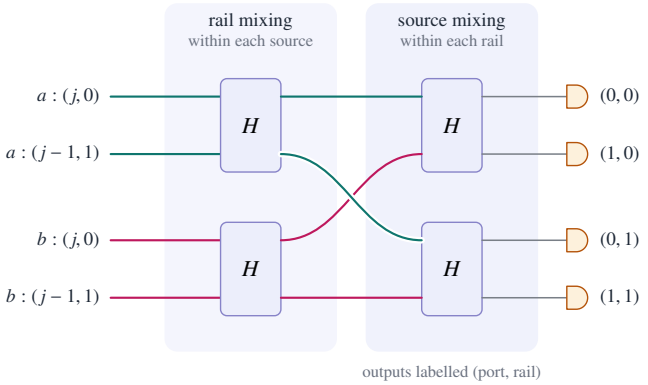


FIG. 5. Balanced four-mode cell in the cyclic network. The first two Hadamard mixers H mix rails within each source; the second two mix sources within each rail. The crossing is a wire permutation, with no coupling at the crossing. Detector labels are (port, rail), in the output order used for b_{loc}.

TABLE III. Exceptional local records, specified by the two detected (port, rail) modes. The last column is the dark subset; m_o is the density normalization factorial.

Rail ℓ	Port 0 collision	Port 1 collision	Split ports
0	$(0,0),(0,0)$	$(1,0),(1,0)$	$(0,0),(1,0)$
1	$(0,1),(0,1)$	$(1,1),(1,1)$	$(0,1),(1,1)$
m_o	2	2	1

in particular, off-diagonal reference coherences are retained. The multiplication includes every routing pattern compatible with the accepted counts.

The helper preparation amplitude is $2^{-(q-1)}$ and the two input Bell pairs supply amplitude $1/2$, giving squared factor 4^{-q}. The local optical entries already include the last two Hadamards. Applying $L_\varsigma^{(q)} = Z_A^{q \bmod 2} X_B^{k_\varsigma}$ and summing the two signs therefore gives the physical accepted J. This proves the formula for all $q \geq 2$. Every positive-semidefinite unit-diagonal Gram has a pure-vector realization, so $J \succeq 0$ follows from this optical construction. In every complete ket and bra assignment each photon occurs once, proving invariance under $\chi_i \mapsto e^{i\theta_i}\chi_i$. Replacing G by $|G|^2$ lacks this derivation and generally gives a different operator.

At each slot, accepted occupation implies $x_{a,j} + x_{b,j} = x_{a,j-1} + x_{b,j-1}$. The 16 states split into nine blocks of sizes $1, 2, 1, 2, 4, 2, 1, 2, 1$. These blocks retain every physical path while reducing contraction work. At fixed Gram input, each realization requires $O(q)$ local contractions; ensemble integration has its own cost.

For a classical product ensemble, linearity of the unnormalized measurement map gives $\bar{J} = \mathbb{E}J$. Taking $\bar{Q}_{\rm err}/\bar{P}$ afterwards automatically accounts for trial-dependent success. This treatment covers separable internal mixed states with an explicit product-ensemble representation. It does not assert a formula for arbitrary internally entangled inputs or for internal states correlated with the logical reference.

3. One-exception and dark records

The one-exception and dark classes below are defined for $q \geq 2$; the $q = 1$ member is used with the uniform bare-BSM rule.

a. *Records and finite-noise counter*

Table III gives all six same-rail count patterns. The two split-port patterns define the dark subset. Every other slot has opposite rails and the same sign ς. All remaining modes have zero counts. There are q locations, two signs and 2^{q-1} ordinary port choices, so $|\mathcal{V}_q| = 6q2^q$ and $|\mathcal{D}_q| = q2^{q+1}$. Neither overlaps the uniform class. For both exceptional classes the recovery is $L_\varsigma^{(q-1)}$, regardless of the exceptional rail, port or location.

Let V_j, D_j be the local sums of (B2) over all six or the two dark patterns, respectively. With j in the ordered list $1, \ldots, q-1, 0$, the needed raw products are

$$\begin{aligned} &[z^1] \prod_{j=1,\ldots,q-1,0} (T_j^{(\varsigma)} + zV_j), \\ &[z^1] \prod_{j=1,\ldots,q-1,0} (T_j^{(\varsigma)} + zD_j). \end{aligned} \tag{B4}$$

The coefficient extraction is exact for noncommuting matrix coefficients because the scalar z commutes and labels exactly one chosen location. Initialize $\mathcal{A}_0 = I, \mathcal{A}_1 = 0$ and update $\mathcal{A}_1' = \mathcal{A}_1 T_j + \mathcal{A}_0 V_j$, $\mathcal{A}_0' = \mathcal{A}_0 T_j$, using old matrices on both right sides. Repeat with D_j for the dark subset. The same data-cut reshape and 4^{-q} factor apply, followed by the exceptional recovery. A two-value counter has constant width, so the contraction still has $O(q)$ sites. Count-legal leakage at finite wave-packet noise is included without imposing the pure-source cancellations below.

b. *Pure-source limits and retention*

For pure same-source packets, conservation of the total route count admits totals zero, one or two. In total one write $x_{a,j} = x_j$, $x_{b,j} = 1 - x_j$. A route flip produces a same-source double occupation. Every ordinary opposite-rail slot forbids it by identical-photon HOM cancellation. A binary cycle cannot have exactly one change, so one exceptional slot cannot create surviving encoding leakage.

In the repetition component, a same-rail record consumes one slot from each source. The remaining repetition strings therefore have length $q-1$, and the known parity phase changes by one. Summing the six detector patterns gives the same-rail projector. Including the same raw preparation cost as the uniform circuit, each location contributes $2^{2-3q}(A^{q-1}\Pi_{\Phi_+} + B^{q-1}\Pi_{\Psi_+})$. The probability for two same-rail photons from the two sources to split ports is $B = (1-u)/2$. Consequently

$$J_{\mathcal{V}_q} = q2^{2-3q}(A^{q-1}\Pi_{\Phi_+} + B^{q-1}\Pi_{\Psi_+}), \qquad J_{\mathcal{D}_q} = BJ_{\mathcal{V}_q}. \tag{B5}$$

Put $S_k = A^k + B^k$ and $c_q = 2^{2-3q}$. For fixed retention $\lambda_{\rm ret} \in [0,1]$, denote the retained rules by subscripts UV and UD. Then

$$\begin{aligned} P_{\rm UV} &= c_q(S_q + \lambda_{\rm ret} q S_{q-1}), \\ Q_{\rm err,UV} &= c_q(B^q + \lambda_{\rm ret} q B^{q-1}), \\ P_{\rm UD} &= c_q(S_q + \lambda_{\rm ret} q B S_{q-1}), \\ Q_{\rm err,UD} &= c_q(1 + \lambda_{\rm ret} q)B^q. \end{aligned} \tag{B6}$$

For fixed $\lambda_{\rm ret} > 0$, the first has $r = q-1$ and the second $r = q$; both have positive ideal probability. The dark class alone has $P|_{u=1} = 0$ and conditional error B^{q-1}/S_{q-1} at $u < 1$. This zero-rate limit is outside the positive-ideal-probability order definition. The scalar relation in Eq. (B5) makes the conditional errors of the individual classes $\mathcal{V}_q$ and $\mathcal{D}_q$ equal for a fixed pure-source overlap.

It does not equate the unions with $\mathcal{U}_q$: their component weights differ. With fluctuating packets there need not be a common scalar proportionality even between the individual operators. Noise-dependent postselection can weight poorly matched realizations more heavily, while the full instrument also includes additional routing contributions. Appendix F 3 compares the individual finite-noise errors and their unions with $\mathcal{U}_q$.

Appendix C: Tangent response, ordering, and calibration

1. Recovering the Laplacian from the finite instrument

For pure source overlap choose $\langle a|b\rangle = c = \sqrt{u} \geq 0$ and a normalized internal mode $g_\perp \perp \mathrm{span}\{a, b\}$. Write $\chi_i = (a_s + z_i g_\perp)/\sqrt{1+|z_i|^2}$, where $a_a = a$ and $a_b = b$. The coefficient vector is ordered as $z = (z_{a,0}, \ldots, z_{a,q-1}, z_{b,0}, \ldots, z_{b,q-1})^T$. Define K_{err} and T_{rate} as the error and total-rate Grams of single-$g_\perp$ amplitudes divided by $P_{\mathcal{U}_q}(u)$. Let P_{cyc} be the cyclic shift, and set

$$L_q = 2I - P_{\mathrm{cyc}} - P_{\mathrm{cyc}}^\dagger, \qquad \mathsf{B}_q = I - L_q/4,$$
$$x_u = (1+u)^{q-1}, \qquad y_u = (1-u)^{q-1},$$
$$d_u = (1+u)^q + (1-u)^q.$$

Expanding the local tensor once in each layer gives

$$K_{\mathrm{err}} = \begin{pmatrix} \frac{x_u}{4d_u} L_q + \frac{y_u}{d_u} I & -\frac{cy_u}{d_u}\mathsf{B}_q \\ -\frac{cy_u}{d_u}\mathsf{B}_q & \frac{x_u}{4d_u} L_q + \frac{y_u}{d_u} I \end{pmatrix},$$
$$T_{\mathrm{rate}} = \begin{pmatrix} \frac{x_u+y_u}{d_u} I & \frac{c(x_u-y_u)}{d_u}\mathsf{B}_q \\ \frac{c(x_u-y_u)}{d_u}\mathsf{B}_q & \frac{x_u+y_u}{d_u} I \end{pmatrix}. \tag{C1}$$

For completeness, the local contractions multiplied by d_u are

Input pair	$d_u[K_{\mathrm{err}}]_{ij}$	$d_u[T_{\mathrm{rate}}]_{ij}$
Same photon	$(x_u + 2y_u)/2$	$x_u + y_u$
Same source, neighbors	$-x_u/4$	0
Opposite sources, same slot	$-cy_u/2$	$c(x_u - y_u)/2$
Opposite sources, neighbors	$-cy_u/4$	$c(x_u - y_u)/4$

A single excitation of the orthogonal mode cannot enable the two opposite-source changes needed to close a nonconstant routing loop. Its two possible exit slots produce the on-site and nearest-neighbor entries; ordinary port sums supply x_u, y_u. For a ket excitation on source a at slot j, the bra excitation on source b contributes twice at j and once at each adjacent slot $j \pm 1$, giving the cross-source table entries in the ratio $2:1:1$. At $q = 2$ the oriented neighbors coincide and their contributions add. The normalization factors of the input states cancel in the conditional ratio, leaving $z^\dagger(K_{\mathrm{err}} - E_{\mathcal{U}_q} T_{\mathrm{rate}})z$. At $u = 1$ and $q \geq 2$, $E_{\mathcal{U}_q} = 0$ and $K_{\mathrm{err}} = (L_q \oplus L_q)/8$.

For multi-direction perturbations, expand $\delta_{s,i} = \sum_\mu z_{s,i,\mu} g_{\perp,\mu}$ in an orthonormal complement of the common ideal packet. For each source and direction, let

$$\mathbf{z}_{s,\mu}^{\pi_s} = (z_{s,\pi_s(0),\mu}, \ldots, z_{s,\pi_s(q-1),\mu})^T$$

list the coefficients in circuit-slot order. Then

$$(\mathbf{z}_{s,\mu}^{\pi_s})^\dagger L_q \mathbf{z}_{s,\mu}^{\pi_s} = \sum_{(i,j)\in\mathcal{E}(\pi_s)} |z_{s,i,\mu} - z_{s,j,\mu}|^2.$$

Distinct single-excitation internal environments are orthogonal, so summing these forms over sources and directions, with the factor $1/8$, proves Eq. (13), including data perturbations. For $q = 2$, the double-edge convention gives the same identity.

2. Equal-spacing ordering

Here $W = W^a + W^b$, $R = F/8$, and $f(k) = w(k\Delta_{\mathrm{em}})$ for integer lag k. The short proof below establishes Eq. (16).

Any cycle visiting all integer positions $0, \ldots, q-1$ has total edge length at least $2(q-1)$. Convexity gives $f(\ell) \geq f(1) + (\ell - 1)[f(2) - f(1)]$ for every positive integer ℓ. Sum this over its q edges and use $f(2) \geq f(1)$ to get the first case of Eq. (16). Folded order has exactly two length-one and $q-2$ length-two edges, attaining equality.

For the concave case put $n = q - 1$ and decompose $f(d) = ad + \sum_{k=1}^{n-1} b_k \min(d, k)$, with $a = f(n) - f(n-1) \geq 0$ and $b_k = 2f(k) - f(k-1) - f(k+1) \geq 0$. The linear cost is at least $2n$. The truncated cost at k is at least $n + k$: if an edge is at least k, it contributes k and the remaining n edges contribute at least one each; otherwise the truncated cost equals the full length, at least $2n \geq n + k$. Natural order has edge lengths $1, \ldots, 1, n$ and attains all these bounds simultaneously.

3. Unequal times and calibration bounds

The classical Supnick and Kalmanson conditions used in the main text are stated with distinct indices; diagonal entries do not constrain a tour. For ordered times $t_0 < \cdots < t_{q-1}$, the resulting costs are

$$F_{\mathrm{n}} = \sum_{j=0}^{q-2} w(t_{j+1} - t_j) + w(t_{q-1} - t_0), \tag{C2}$$

$$F_{\mathrm{f}} = w(t_1 - t_0) + w(t_{q-1} - t_{q-2}) + \sum_{j=0}^{q-3} w(t_{j+2} - t_j). \tag{C3}$$

For four chronological points with gaps a, b, c, monotonicity yields $w(a) + w(c) \leq w(a+b) + w(b+c)$. Convexity gives $w(a+b) + w(b+c) \leq w(a+b+c) + w(b)$; concavity reverses the latter inequality. These are the four-point

conditions under which the classical results of Refs. [22–24] give the natural and folded shortest tours.

Let A^{π}_{ij} count cycle edges with unordered endpoints $i < j$; the two-vertex cycle has multiplicity two. Let $\Delta = F_{\mathrm{f}} - F_{\mathrm{n}}$, so a negative value favors folded wiring. Given calibrated cost estimates $\widehat{W}_{ij}$ and valid absolute errors b_{ij}, the natural–folded comparison has

$$\widehat{\Delta} = \sum_{i<j} (A^{\mathrm{f}}_{ij} - A^{\mathrm{n}}_{ij})\widehat{W}_{ij}, \qquad |\Delta - \widehat{\Delta}| \le \sum_{i<j} |A^{\mathrm{f}}_{ij} - A^{\mathrm{n}}_{ij}| b_{ij}.$$

Use the upper bound on each left side and the lower bound on each right side to certify a four-point condition. If neither ordering condition is certified, the difference bound only compares these two candidate tours. Estimated sampling standard errors (SEs) do not by themselves constitute valid absolute bounds. If the input is a finite-noise HOM proxy, a rigorous optical leading-cost claim also needs its approximation error in b_{ij}.

These bounds can be applied to model-generated calibration matrices. For example, unequal emission times $t/\Delta_{\mathrm{em}} = (0, 0.6, 1.8, 3.1, 4.7)$, unequal source slow amplitudes, and unequal independent variances give folded candidates for a smooth kernel and natural candidates for OU. These are synthetic examples; spectra and higher noise statistics must be characterized separately for a device prediction.

For Gaussian center frequencies, a same-source pair with mean difference $\Delta\mu$ and difference variance v has

$$\mathbb{E}V_{ij} = \frac{\exp[-(\Delta\mu)^2/(4\sigma^2 + 2v)]}{\sqrt{1 + v/(2\sigma^2)}}. \tag{C4}$$

For constant source mean, $v = 2\sigma_d^2[1 - \mathcal{R}(t_i - t_j)] + \sigma_{f,i}^2 + \sigma_{f,j}^2$. This supplies the illustrative calibration values without internal-mode truncation.

An explicit Gaussian tangent convention is $\Omega_i = \Omega_0 + \xi\omega_i$ about a common center. It gives $\delta_i = \omega_i \partial_\Omega \chi_\Omega|_{\Omega_0}$ and

$$\|\delta_i - \delta_j\|^2 = \frac{(\omega_i - \omega_j)^2}{4\sigma^2}. \tag{C5}$$

If the independent part of ω_i has variance v_f^2, its leading Bell error is $\xi^2 q v_f^2/(8\sigma^2)$. Writing the actual small frequency variance as $\sigma_f^2 = \xi^2 v_f^2$ recovers the main-text coefficient. The finite ensemble at separated nominal centers uses the full Gram matrix, not this common-center expansion.

Appendix D: Scalar loss and synchronization

For a core of M modes, append two M-mode vacuum environments. On core and the first environment use the diagonal beam-splitter transformation

$$B(T) = \begin{pmatrix} \sqrt{T} & \sqrt{I-T} \\ -\sqrt{I-T} & \sqrt{T} \end{pmatrix},$$

$$T_{s,j,\ell;s,j,\ell} = \eta_{\mathrm{route},i} e^{-\kappa(q-1-j)\Delta_{\mathrm{em}}}.$$

Here i labels the setting and $q = q_i$. The two logical rails have the same transmission, and columns are indexed by chronological emission, before the static permutation. Embed $B(T)$ into $3M$ modes, apply $\mathrm{diag}(U_\pi, I_M, I_M)$, then mix the core with the second vacuum environment using $B(\eta I_M)$. This is a complete passive unitary dilation. With N photons supplied and no false counts, every accepted core record has N photons, so both environments must be vacuum. Its Kraus factor is independent of logical input because each emission supplies one photon and both rails have equal transmission. The density factor is

$$\eta^{2q} \prod_{s,j} \eta_{\mathrm{route},i} e^{-\kappa(q-1-j)\Delta_{\mathrm{em}}} = \eta^{2q} \eta_{\mathrm{route},i}^{2q} e^{-\kappa q(q-1)\Delta_{\mathrm{em}}}. \tag{D1}$$

Vacuum environment modes add no supplied photons. The same argument applies to the Fourier comparator with its actual source/time input mapping.

This dilation describes the stated serial waiting model with frequency-flat attenuation and equal transmission on the logical rails. Frequency-dependent filtering, dispersion, dark counts, and dephasing can be incorporated through additional device models. Temporal-to-spatial loading can require active clocked hardware [25]; the selected spatial assignment is still fixed and independent of hidden noise. If an additional loading step is frequency-flat, logical-rail independent and has uniform per-photon survival η_{load}, every setting's $P_{\mathrm{det},i}$ gains $\eta_{\mathrm{load}}^{N_i}$. Recompute the entire frontier afterwards.

Random setting selection assumes its preparation and switching overhead is already in the supplied-photon interface model. If overhead is setting dependent, modify that setting's $N_i, P_{\mathrm{det},i}, J_i$ first. If it depends on transitions between settings, the independent-attempt cost theorem does not automatically price those transitions; long predetermined batches can avoid per-trial switching but may need their own drift-stationarity check.

Appendix E: Six-photon Fourier comparator

1. Network and specified acceptance sets

For six photons, let $\zeta_6 = e^{2\pi i/6}$ and define the spatial Fourier matrix $[\mathsf{F}_6]_{ok} = \zeta_6^{ok}/\sqrt{6}$ for $o, k = 0, \ldots, 5$. The full 10×10 comparator unitary has data columns $0, 1$ for source a and $2, 3$ for source b, helper columns $4, 5$ from source a and $6, 7$ from source b, and vacuum columns $8, 9$. At $t_{\mathrm{mix}} = 1/3$, put $(k_i) = (0, 1, 4, 3, 3, 4, 0, 1)$. For rows $o = 0, \ldots, 5$, use

$$U_{oi} = \begin{cases} \zeta_6^{ok_i}\sqrt{t_{\mathrm{mix}}/6}, & i < 4, \\ \zeta_6^{ok_i}\sqrt{(1 - t_{\mathrm{mix}})/6}, & 4 \le i < 8, \end{cases}$$
$$U_{o8} = \zeta_6^{2o}/\sqrt{6}, \qquad U_{o9} = \zeta_6^{5o}/\sqrt{6}. \tag{E1}$$

The remaining rows pair $(d, h) = (0, 6), (1, 7), (2, 5), (3, 4)$ in that order: $U_{o,d} = \sqrt{1 - t_{\mathrm{mix}}}$, $U_{o,h} = -\sqrt{t_{\mathrm{mix}}}$ for

$o = 6, 7, 8, 9$; all their other entries vanish. Each pair first splits into a bright Fourier column and a complementary reject row, proving unitarity. Set $\mathcal{Q}_0$ accepts only $y_0 = (1, 1, 1, 1, 1, 1, 0, 0, 0, 0)$ with recovery Z_A.

Every count below has four terminal zeros. The following table completely specifies the additional fixed sets; y_0 is always accepted with weight one and recovery Z_A. Unlisted records are rejected.

Set	Additional first six counts	Acceptance	Recovery
$\mathcal{Q}_1$	$(1, 2, 0, 1, 2, 0)$	0.03836549	Z_A
$\mathcal{Q}_2$	$(0, 2, 1, 0, 2, 1)$	0.003393931	Z_A
$\mathcal{Q}_3$	$(0, 2, 1, 0, 2, 1)$	0.04236057	Z_A
$\mathcal{Q}_4$	$(2, 0, 2, 0, 2, 0)$	1	I
	$(0, 2, 0, 2, 0, 2)$	1	I
	$(0, 1, 2, 0, 1, 2)$	0.4105456	Z_A

The comparator uses the fixed unitary and acceptance rules specified above. The full-precision unitary, input columns, retention probabilities, count patterns, and raw Bell targets are provided in `data/fourier.json`. The corresponding local recoveries are constructed by `target_recovery` in `src/accepted_records.py`. The physical emission mapping is a_0, b_0 for the data and a_1, a_2, b_1, b_2 for their ordered helpers. All use the same frequency distribution, timing, detection efficiency and serial storage model as the cyclic settings.

2. General Gram polynomial and analytic Gaussian average

For a complete record y, repeat its output rows and let U_l be the $N \times N$ matrix for logical reference index l, with photons in source-grouped chronological order. For a relative permutation ϑ in the permutation group S_N, the double-permanent expansion reorganizes to

$$[J_y^{\mathrm{raw}}]_{lk} = \sum_{\vartheta \in S_N} \frac{\mathrm{per}(U_l \odot \overline{U_k[:, \vartheta]})}{4 m_y} \prod_{i=0}^{N-1} G_{\vartheta(i),i}. \quad \text{(E2)}$$

Here $m_y = \prod_j y_j!$, $\odot$ denotes entrywise multiplication, and $U_k[:, \vartheta]$ permutes the input columns by ϑ. To verify the indexing, fix a ket assignment π and bra assignment φ, and set $\vartheta = \varphi \circ \pi^{-1}$ on photon labels. The Gram monomial depends only on ϑ; summing π yields the displayed permanent. The $1/4$ is the input Bell-pair density factor; preparation is already in U. Apply each actual recovery, multiply by its acceptance, and sum the coefficient matrices once for an entire fixed set. For $N = 6$ there are only $6! = 720$ relative permutations, irrespective of the number of noise points.

For Gaussian frequency vector $\Omega \sim \mathcal{N}(\mu, \Sigma)$ write $\Sigma = S_\Sigma S_\Sigma^T$. Define the permutation matrix by $[\Pi_\vartheta \Omega]_i = \Omega_{\vartheta(i)}$. Let $D_\vartheta = \Pi_\vartheta - I$, $A_\vartheta = D_\vartheta^T D_\vartheta / (4\sigma^2)$, $B_\vartheta = I + S_\Sigma^T A_\vartheta S_\Sigma$ and $b_\vartheta = S_\Sigma^T A_\vartheta \mu$. Completing the Gaussian square gives

$$\mathbb{E} \prod_i G_{\vartheta(i),i} = \frac{\exp[-(\mu^T A_\vartheta \mu - b_\vartheta^T B_\vartheta^{-1} b_\vartheta)/2]}{\sqrt{\det B_\vartheta}}. \quad \text{(E3)}$$

This also permits singular covariance with a positive-semidefinite square root. The average is analytic up to floating-point arithmetic, with all coefficients determined by the specified unitary and acceptance rule.

Appendix F: Numerical methods, frontiers, and controls

1. Integration and numerical uncertainty

The primary Gaussian averages use eight independent randomized Sobol scrambles of 2^{12} points per q; the three controls use four scrambles of 2^{10} points. Both wirings and all acceptance classes share frequency samples at fixed q. For replicate operators J_b, let $P_b = \mathrm{Tr}\, J_b$ and $Q_b = \mathrm{Tr}(\Pi_\perp J_b)$. The estimated standard error of $\bar{E}$ is the sample standard deviation of $(Q_b - \bar{E} P_b)/\bar{P}$, divided by the square root of the scramble count. This retains rate correlations.

For the relative wiring change, define $d = \bar{E}_{\mathrm{f}}/\bar{E}_{\mathrm{n}} - 1$, using each ratio of mean error weight to mean success. With n_{scr} scrambles, delete the same scramble b from both wirings and compute $d_{(-b)} = \bar{E}_{\mathrm{f},(-b)}/\bar{E}_{\mathrm{n},(-b)} - 1$. The paired jackknife standard error is

$$\mathrm{SE}(d) = \left[\frac{n_{\mathrm{scr}} - 1}{n_{\mathrm{scr}}} \sum_b (d_{(-b)} - \overline{d}_{(-)})^2 \right]^{1/2}, \quad \text{(F1)}$$

where $\overline{d}_{(-)}$ is the mean of the delete-one values. Multiplication by 100 gives percentage points; the paired values are reported below. These estimates measure numerical integration variability, not uncertainty in the physical source parameters.

Independent eight-scramble, 8192-point estimates for the decisive uniform $q = 4, 5$ settings give Table IV. The main figures and frontiers use the primary means. For the refinement, only these decisive uniform means are replaced before reoptimizing, while all other catalog entries are held fixed. An independent natural $q = 3, \mathcal{U}_q \cup \mathcal{V}_q$ estimate changes its error by relative 1.6×10^{-5}, with refined standard error 2.11×10^{-7} in absolute infidelity.

TABLE IV. Pooled costs at τ_*. Primary uses 4096 points per scramble; refinement replaces only decisive uniform means with independent 8192-point estimates. Both use eight scrambles. Full-precision values are provided in the data.

Means	Ref. $C/10^4$	Exp. $C/10^4$	Ratio
Primary	15.936	2.863	5.57
Refinement	15.686	2.863	5.48

An adverse shift moves reference errors down and rates up by six estimated standard errors, and expanded errors up and rates down, before reoptimization. The ratio is about 5.17; this is a numerical stress test, not a confidence bound. Sixteen calibration corners vary slow amplitude

TABLE V. Primary pooled policies at τ_*: attempt probabilities a_i and successful-event weights w_i. Cycle components use the uniform rule. Mean supplied photons per attempt are 9.71 (reference) and 7.89 (expanded).

Set	Component	a_i	w_i
Ref.	Natural $q = 5$	0.8559	0.3491
Ref.	Natural $q = 4$	0.1441	0.6509
Exp.	Folded $q = 4$	0.9457	0.9072
Exp.	Fourier $\mathcal{Q}_0$	0.0543	0.0928

TABLE VI. Fourier-comparator optical acceptance and error in the primary ensemble. All five sets remain in both catalogs. These are analytic Gaussian averages, with floating-point arithmetic error but no Monte Carlo sampling uncertainty.

Set	$10^4\bar{P}$	$10^4\bar{E}$
$\mathcal{Q}_0$	8.9698	7.2954
$\mathcal{Q}_1$	9.1268	11.6565
$\mathcal{Q}_2$	8.9837	7.6873
$\mathcal{Q}_3$	9.1432	12.1020
$\mathcal{Q}_4$	12.9757	99.4665

TABLE VII. Fixed-size percentage changes $100(\bar{E}_{\mathrm{f}}/\bar{E}_{\mathrm{n}} - 1)$, with paired numerical standard errors in percentage points. Primary: eight scrambles; controls: four. These are integration uncertainties, not device confidence intervals.

Model	$N = 8$	$N = 10$
Smooth	-7.948 ± 0.002	-22.835 ± 0.002
OU	$+2.045 \pm 0.022$	$+5.008 \pm 0.033$
Short correlation	-0.477 ± 0.020	$+5.936 \pm 0.019$
Higher floor	-5.236 ± 0.016	-13.715 ± 0.022

TABLE VIII. Individual one-exception and dark-class errors under the primary finite-noise model. These are the individual component classes $\mathcal{V}_q$ and $\mathcal{D}_q$, not their unions with $\mathcal{U}_q$.

q	Wiring	$10^4\bar{E}_{\mathcal{V}_q}$	$10^4\bar{E}_{\mathcal{D}_q}$
4	Natural	19.361	34.740
4	Folded	18.704	32.421
5	Natural	9.389	28.389
5	Folded	7.562	22.104

and correlation time by ±1%, fast amplitude by ±10%, and u_{nom} by ±0.0002. The $q = 4$ error ratio stays in $[0.91886, 0.92210]$. Folded $q = 4$ meets τ_* at all corners, natural $q = 4$ meets it at five, and natural $q = 5$ fails at four. These discrete checks do not certify a continuous parameter region or a uniform cost ratio.

The transfer implementation has independent small-q complete optical-state checks. At $q = 3$, direct propagation with complex two-dimensional packets includes all 144 exceptional records and 48 dark members, with collision normalization $\sqrt{\prod_o y_o!}$ in amplitudes. Normalized full-operator discrepancies are below 6×10^{-16}. The four additional Fourier sets agree with independent propagation to below 9×10^{-16}. These floating-point checks concern the optical formulas; they are separate from physical integration uncertainty.

2. Finite-catalog optimization and policies

There are 35 natural cycle settings, 35 folded cycle settings, five Fourier sets, and bare BSM: 41 reference and 76 expanded settings. Dark classes are included at their nonzero finite-noise probabilities. The common options, timing, and cost model are those of Sec. V. For successful-event weights the optimization is

$$\min_{w_i \geq 0} \sum_i w_i C_i, \qquad \sum_i w_i = 1, \qquad \sum_i w_i e_i \leq \tau. \quad \text{(F2)}$$

An optimum has at most two nonzero weights. A line $C = a + bE$, $b \leq 0$, below all points gives the dual bound $C \geq a + b\tau$; both supports saturate it at a two-setting optimum. Rational arithmetic verifies the supporting-line inequalities exactly for the tabulated decimal estimates. Equation (26) gives the attempt probabilities; Table V lists the primary target policies.

Within one optical network, choosing $\mathcal{U}_q$ or $\mathcal{U}_q \cup \mathcal{V}_q$ before a trial is equivalent to retaining exceptional records with fixed probability λ_{ret}. The declared fixed-network families optimize at approximately 0.00325 for natural $q = 5$ and 0.00474 for folded $q = 4$. This realizes the middle row of Table II.

From the strictest feasible target toward looser targets, the first two pooled supports are natural uniform $q = 5, 4$ for reference and folded uniform $q = 5, 4$ for expanded. The remaining common sequence is $\mathcal{Q}_0$, natural uniform $q = 3$, natural $q = 3$ with $\mathcal{U}_q \cup \mathcal{V}_q$, natural uniform $q = 2$, natural $q = 2$ with $\mathcal{U}_q \cup \mathcal{V}_q$, and bare BSM. None of $\mathcal{Q}_1, \ldots, \mathcal{Q}_4$ or the dark extensions enters this primary support. The Fourier-comparator errors are evaluated under the same ensemble (Table VI).

3. Operating boundaries

Table VII gives the paired fixed-size error changes. Table VIII lists the individual one-exception and dark components separately from their unions with $\mathcal{U}_q$. Figure 6 shows the complete q dependence of the three controls, with the primary model shown faintly for comparison. The OU minimum error is 1.10×10^{-3} and the short-correlation minimum is 1.16×10^{-3}. Both are attained by Fourier $\mathcal{Q}_0$, and the reference and expanded pooled frontiers coincide. At $\sigma_f/\sigma = 0.02$ their minima are 6.66×10^{-4} and 6.11×10^{-4}. Both exceed the common target despite the fixed-size quality improvement. Scalar losses preserve these conditional errors but determine the photon costs.

Figure 7 compares the unions, whose component success weights determine their conditional errors. At finite

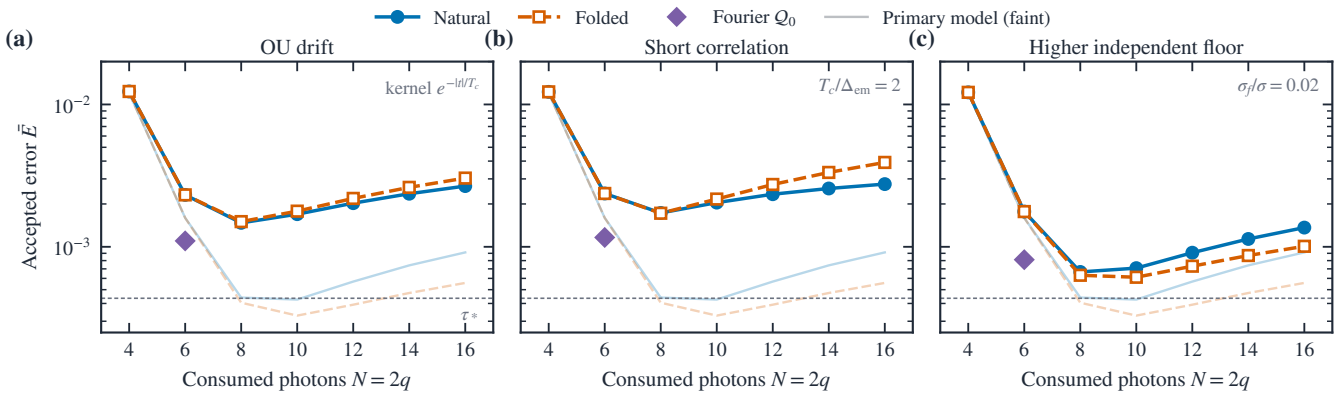


FIG. 6. Errors under the uniform acceptance rule for three controls, with the primary model shown faintly, shared vertical limits, and fixed emission spacing. Each control changes only the quantity stated in Fig. 3. The diamond is Fourier $\mathcal{Q}_0$ and the dotted line is τ_*. Error bars are per-setting numerical scramble standard errors. Natural wiring uses filled circles and solid lines; folded wiring uses open squares and dashed lines.

noise the instrument also includes every count-compatible route. Figure 4(a) shows where the unions enter the full target range.

4. Analytic spectral-filter comparison

Consider the common amplitude filter of Sec. V E, with unit peak intensity transmission, identical response on both logical rails, and $\omega_F = (\mu_a + \mu_b)/2$. Multiplication of the Gaussian amplitudes in Eq. (21) gives a packet of width $\sigma\sqrt{s_F}$ and center $s_F\Omega + (1 - s_F)\omega_F$, where

$$s_F = \frac{\sigma_F^2}{\sigma^2 + \sigma_F^2},$$
$$T_F(\Omega) = \sqrt{s_F}\exp\left[-\frac{(1 - s_F)(\Omega - \omega_F)^2}{2\sigma^2}\right]. \tag{F3}$$

Here T_F is the single-photon transmission probability, not an amplitude. For fixed pure source packets, their filtered squared overlap is u^{s_F} and the joint transmission is $s_F u^{1-s_F}$ [18]. Bare BSM has conditional acceptance 1/2, hence

$$E_F = \frac{1 - u^{s_F}}{2}, \qquad C_F = \frac{4}{\eta^2 s_F u^{1-s_F}}. \tag{F4}$$

All failed filter attempts consume the two supplied photons and are charged.

For the primary ensemble, the two source frequencies are independent Gaussians with equal variance $\sigma_d^2 + \sigma_f^2$. Set $g_F = (\sigma_d^2 + \sigma_f^2)/\sigma^2$, $h_F = -\log u_{\rm nom}$, $D_F = 1 + (1 - s_F)g_F$, and $K_F = 1 + g_F$. Define the filtered squared overlap $u_F = \exp[-s_F(\Omega_a - \Omega_b)^2/(4\sigma^2)]$ and the joint mean transmission $\overline{\mathcal{T}}_F = \mathbb{E}[T_F(\Omega_a)T_F(\Omega_b)]$. Integrating each Gaussian after multiplying by its transmission gives

$$\overline{\mathcal{T}}_F = \frac{s_F}{D_F}\exp[-(1 - s_F)h_F/D_F],$$
$$\frac{\mathbb{E}[T_F(\Omega_a)T_F(\Omega_b)u_F]}{\overline{\mathcal{T}}_F} = \sqrt{\frac{D_F}{K_F}}\exp[-s_F h_F/(D_F K_F)],$$
$$\bar{E}_F = \frac{1}{2}\left[1 - \sqrt{\frac{D_F}{K_F}}e^{-s_F h_F/(D_F K_F)}\right],$$
$$C_F = \frac{4}{\eta^2 \overline{\mathcal{T}}_F}. \tag{F5}$$

One way to verify the integration is to use the center sum and difference: these are independent Gaussians, and transmission reweights both before the overlap is averaged. This is the same successful-trial normalization as Eq. (3).

At $g_F = 0.010025$ and $\tau_* = 4.35 \times 10^{-4}$ the solution is $s_F = 0.00411468$, $\sigma_F/\sigma = 0.06428$, and mean single-photon transmission 0.05753. Thus $C_F = 1492.08$ with the same $\eta = 0.9$; the expanded and reference pooled costs are respectively 19.19 and 106.80 times larger. A 32×32 Gauss–Hermite evaluation of the weighted integral checks the analytic expression. Extra frequency-flat filter peak intensity efficiency ζ_F would multiply C_F by ζ_F^{-2}. None is imposed in this comparison.

Figure 8 compares the two strategies for pure source packets.

With no storage or extra routing loss, let

$$\kappa_{\rm pure} = \frac{\log[8/(\eta^2 A)]}{\log(A/B)}. \tag{F6}$$

Choosing the smallest integer q that meets a strict target gives $q = O(\log(1/\tau))$ and $C_{\mathcal{U}_q} = O(\log(1/\tau)\tau^{-\kappa_{\rm pure}})$, with bounded factors from rounding q. By contrast Eq. (F4) scales as τ^{-1} for fixed $0 < u < 1$. The ex-

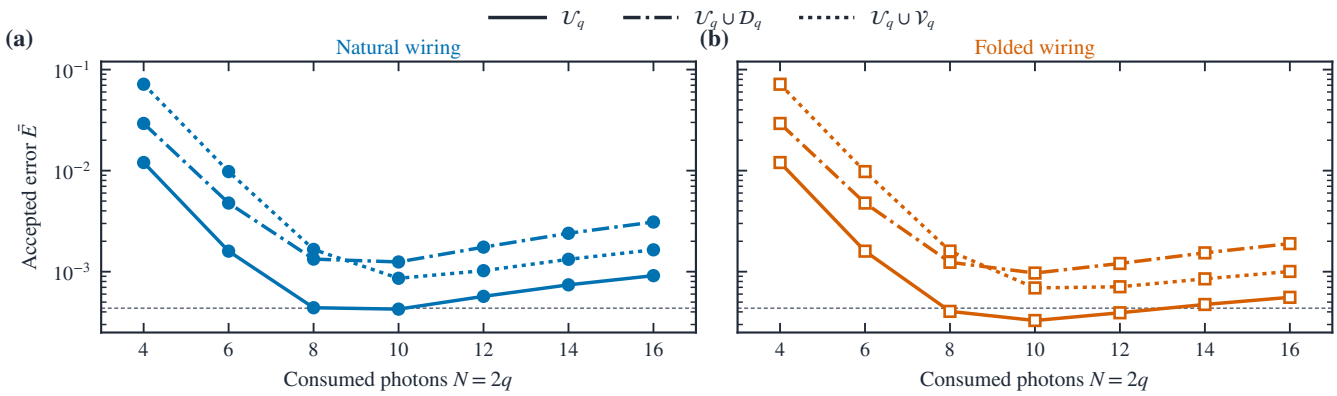


FIG. 7. Uniform and union acceptance rules under the primary Gaussian ensemble, shown on a common vertical scale. Color and marker encode wiring; line style encodes $\mathcal{U}_q$, $\mathcal{U}_q \cup \mathcal{D}_q$, or $\mathcal{U}_q \cup \mathcal{V}_q$. Each union includes the uniform records as well as its additional class; its error includes success weighting and all count-compatible routes. Error bars denote numerical scramble standard errors.

ponent condition is exactly

$$\kappa_{\mathrm{pure}} < 1 \quad \Longleftrightarrow \quad 8\epsilon < \eta^2(1-\epsilon)^2. \tag{F7}$$

At $\eta = 0.9$ it requires $\epsilon < 0.0848051$. The exponents are 1.0603 at $u = 0.81$ and 0.5006 at $u = 0.98$. This is an asymptotic statement for the specified pure-source models, not a ranking at every finite target. The primary storage penalty $\exp[0.002q(q-1)]$ and finite-noise floor prevent applying that asymptote to the primary ensemble. At targets above the bare error, both strategies may simply use bare BSM.

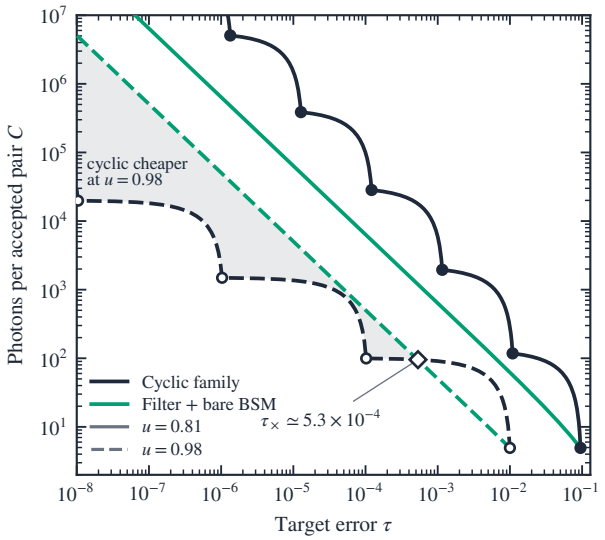


FIG. 8. Pure-source comparison with an internal-state-selective filter. At $\eta = 0.9$, zero drift and no storage or extra routing loss, the uniform cyclic catalog $q = 1, \ldots, 8$ is pooled in physical linear (E, C) and compared with a common Gaussian filter followed by bare BSM. Solid lines and filled markers denote $u = 0.81$; dashed lines and open markers denote $u = 0.98$. Points are individual cyclic settings. For $u = 0.98$, shading shows where the displayed cyclic frontier has lower photon cost, and the diamond marks the crossing $\tau_\times \simeq 5.3 \times 10^{-4}$. The cyclic comparison is restricted to the reachable range of the displayed $q \leq 8$ catalog. Filter rejection is included, with unit peak intensity transmission on both rails.

5. Notation guide

Table IX groups the central symbols and points to their first definitions; local tensor indices remain in Appendix B.

TABLE IX. Notation by role. A bar denotes averaging the unnormalized operator before normalization.

Symbol	Meaning	First definition
$R_A, R_B;\ \Psi_{\mathrm{in}}$	Retained references and joint input	Eq. (1)
u, ϵ	Pure-source squared overlap; bare mismatch error $(1-u)/2$	Sec. II A
$J_y, J;\ P, Q_{\mathrm{err}}, E$	Unnormalized record/accepted states; probability, error weight, infidelity	Eq. (2)
$\Pi_{\Phi_\pm}, \Pi_\perp, \Pi_{\Psi_+}$	Target, error, and second Bell projectors	Eqs. (2), (8)
$\bar{J}, \bar{P}, \bar{E}$	Successful-trial ensemble quantities	Eq. (3)
$n_s, N;\ r, q$	Per-source and total photons; suppression order and slots per source	Secs. II, III
$\eta, s_{\mathrm{loss}}, P_{\mathrm{det}}, C$	Detection efficiency, scalar survival, detected success probability, photons per accepted pair	Eq. (4)
a_i, w_i, e_i	Attempt/success weights and setting error	Sec. V C
τ	Target conditional infidelity	Sec. V C; Eq. (F2)
$U_{\mathrm{cyc}}, H, C_s, B_{\mathrm{cross}}$	Complete passive circuit and its balanced/routing layers	Eq. (6)
y, γ_y, L_y	Complete count pattern, retention and local recovery	Eq. (2)
$\mathcal{U}_q, \mathcal{V}_q, \mathcal{D}_q;\ \mathcal{Q}_k$	Uniform, one-exception, dark, and Fourier acceptance classes	Secs. III A, V B
A, B, c_q	$(1+u)/2, (1-u)/2, 2^{2-3q}$	Eq. (8)
$G, T_j^{(\varsigma)}, \mathcal{B}_q$	Photon Gram, local transfer and boundary readout	Eq. (11)
m_y, m_o	Complete and local occupation factorials	Apps. A, B
$P_{\mathrm{cyc}}, L_q, \mathsf{B}_q$	Cyclic shift, Laplacian and $I - L_q/4$	Eq. (C1)
$t_{\mathrm{mix}}, \varphi, \vartheta$	Fourier splitter fraction; bra and relative permutations	Eqs. (E1), (E2)
$\xi, \delta_{s,i}, \pi_s, \mathcal{E}$	Dimensionless tangent expansion, assignment and cycle edges	Eqs. (12), (13)
W^s, W, F, R	Source/combined edge weights, cycle cost and Bell coefficient	Eq. (14)
$g_q(k)$	Normalized leading delay cost; comparison of two tours	Eqs. (17), (18)
$v_{s,i}, c_\nu, \nu$	Independent tangent variance; power-law coefficient and exponent	Eqs. (15), (19)
Ω, ω, σ	Center frequency, spectral coordinate, intensity width	Eq. (21)
$\sigma_d, \sigma_f, \mathcal{R}, T_c$	Slow/independent frequency noise, correlation kernel/time	Sec. V A
$\Delta_{\mathrm{em}}, T, \kappa$	Emission spacing, batch window, attenuation rate	Eqs. (19), (24)
H_F, σ_F	Amplitude response and filter width	Sec. V E
s_F, T_F	Narrowed variance fraction and transmission probability	Eq. (F3)
g_F, h_F, D_F, K_F	Dimensionless finite-noise integration parameters	Eq. (F5)
κ_{pure}	Pure, zero-storage asymptotic cost exponent	Eq. (F6)

[1] L. Bianchi, C. Marconi, and D. Bacco, Bell state measurements in quantum optics: a review of recent progress and open challenges, Quantum Sci. Technol. **11**, 023001 (2026).

[2] H.-J. Briegel, W. Dür, J. I. Cirac, and P. Zoller, Quantum repeaters: The role of imperfect local operations in quantum communication, Phys. Rev. Lett. **81**, 5932 (1998).

[3] D. Main, P. Drmota, D. P. Nadlinger, E. M. Ainley, A. Agrawal, B. C. Nichol, R. Srinivas, G. Araneda, and D. M. Lucas, Distributed quantum computing across an optical network link, Nature **638**, 383 (2025).

[4] L. Zhai *et al.*, Quantum interference of identical photons from remote GaAs quantum dots, Nature Nanotechnology **17**, 829 (2022).

[5] A. Thoma *et al.*, Exploring dephasing of a solid-state quantum emitter via time- and temperature-dependent Hong–Ou–Mandel experiments, Phys. Rev. Lett. **116**, 033601 (2016), arXiv:1507.05900.

[6] J. Marshall, Distillation of indistinguishable photons, Phys. Rev. Lett. **129**, 213601 (2022).

[7] C. F. D. Faurby *et al.*, Purifying photon indistinguishability through quantum interference, Phys. Rev. Lett. **133**, 033604 (2024).

[8] J. Saied, J. Marshall, N. Anand, and E. G. Rieffel, General protocols for the efficient distillation of indistinguishable photons, Phys. Rev. Applied **23**, 034079 (2025), arXiv:2404.14217.

[9] F. H. B. Somhorst, B. K. Sauër, S. N. van den Hoven, and J. J. Renema, Photon-distillation schemes with reduced resource costs based on multiphoton Fourier interference, Phys. Rev. Applied **23**, 044003 (2025).

[10] F. H. B. Somhorst *et al.*, Below-threshold error reduction in single photons through photon distillation (2026), arXiv:2601.05947.

[11] F. Hoch *et al.*, Optimal distillation of photonic indistinguishability, Phys. Rev. Research 10.1103/lyw5-qdfx (2026), to be published, arXiv:2509.02296.

[12] S.-W. Lee, K. Park, T. C. Ralph, and H. Jeong, Nearly deterministic Bell measurement for multiphoton qubits and its application to quantum information processing, Phys. Rev. Lett. **114**, 113603 (2015).

[13] S. D. Reiß and P. van Loock, Optimal logical Bell measurements on stabilizer codes with linear optics, Phys. Rev. A **114**, 032421 (2026), arXiv:2601.08820.

[14] S. N. van den Hoven, G. B. Lamers, and J. J. Renema, Photonic fusion operations transform partial distinguishability (2026), arXiv:2609.01019.

[15] S. Bartolucci *et al.*, Beyond fidelity: Resolving errors in photonic seed state generation (2026), arXiv:2610.26603.

[16] J.-W. Pan, C. Simon, C. Brukner, and A. Zeilinger, Feasible entanglement purification for quantum communication, Nature **410**, 1067 (2001), arXiv:quant-ph/0012026.

[17] Y. Sagi, Scheme for generating Greenberger-Horne-Zeilinger-type states of n photons, Phys. Rev. A **68**, 042320 (2003), arXiv:quant-ph/0307097.

[18] A. Chen, A mode-mixing threshold for entanglement swapping with one independent auxiliary photon (2026), zenodo preprint.

[19] V. S. Shchesnovich, Partial indistinguishability theory for multiphoton experiments in multiport devices, Phys. Rev. A **91**, 013844 (2015).

[20] A. J. Menssen, A. E. Jones, B. J. Metcalf, M. C. Tichy, S. Barz, W. S. Kolthammer, and I. A. Walmsley, Distinguishability and many-particle interference, Phys. Rev. Lett. **118**, 153603 (2017).

[21] D. Cilluffo, M. Kost, N. Lorenzoni, and M. B. Plenio, Heisenberg picture tensor network formalism for optical circuits, Phys. Rev. Research **8**, 023098 (2026).

[22] F. Supnick, Extreme Hamiltonian lines, Annals of Mathematics **66**, 179 (1957).

[23] K. Kalmanson, Edgeconvex circuits and the traveling salesman problem, Canadian Journal of Mathematics **27**, 1000 (1975).

[24] V. G. Deineko, J. A. van der Veen, R. Rudolf, and G. J. Woeginger, Three easy special cases of the Euclidean travelling salesman problem, RAIRO Recherche Opérationnelle **31**, 343 (1997).

[25] J. Münzberg *et al.*, Fast and efficient demultiplexing of single photons from a quantum dot with resonantly enhanced electro-optic modulators, APL Photonics **7**, 070802 (2022), arXiv:2203.08682.

[26] D. Bertsimas and J. N. Tsitsiklis, *Introduction to Linear Optimization* (Athena Scientific, Belmont, Massachusetts, 1997).

[27] A. Chen, Arbitrary-order suppression of source mismatch in photonic entanglement swapping: code and data (2026), zenodo, software release V0.14.3.

[28] N. Ghareghani, E. Ghorbani, and M. Mohammad-Noori, Intersection matrices revisited, J. Combin. Des. **20**, 383 (2012), arXiv:0902.4367.

[29] A. Chen, Fidelity limits and purity requirements for entanglement swapping with one auxiliary photon (2026), zenodo preprint.